

Physics-based Long-term Geomagnetic Indices

L. Svalgaard, Easy Toolkit, Inc, 6927 Lawler Ridge, Houston, TX 77055, USA.
(leif@leif.org)

E. W. Cliver, Air Force Research Laboratory, Hanscom AFB, MA 01731, USA.
(Edward.Cliver@hanscom.af.mil)

Abstract

A geomagnetic index aims to be a summary of certain aspects of the very complex phenomenon of geomagnetic activity. Many geomagnetic indices have been proposed and used over the years. As so strongly emphasized already by J. Bartels and re-iterated by P.N. Mayaud, a given geomagnetic index should monitor a single class of geomagnetic variations stemming from a definite physical cause. There are many indices for which this goal is not reached (e.g. the classical daily range indices and the modern *Dst* index). Preferably, an index should be simple to derive without requiring elaborate empirical conversion or adjustment tables and be reproducible by automatic means. Many indices do not meet these criteria (e.g. the *Kp*, *am*, and *PC* indices). There has been a tendency to increase the time-resolution of the indices (e.g. from hours to minutes). Little is gained by this: the summary aspects are overwhelmed by the vastly increased data volume which typically is available for a much shorter time interval, several additional phenomena intrude (e.g. micropulsations), and time- and length scales often no longer match the scales for the physical causes to be monitored. Certain phenomena occur chiefly on the dayside of the magnetosphere (e.g. solar flare effects, the 'regular' solar quiet-time thermal wind and tide effects, sudden storm commencements, the Svalgaard- Mansurov effect) and have physical causes distinct from the 'classical' geomagnetic activity that peaks near midnight.

We discuss new geomagnetic indices based on nighttime data only, thus avoiding (rather than attempting to solve by ad-hoc methods) the problem of 'mixing-in' of the daytime effects. Using stations distributed in longitude, continuous coverage in Universal Time is obtained:

1) The Inter-Hour-Variability (*IHV*-) index is defined as the sum of the six unsigned differences between seven successive hourly means (of the H-component of the geomagnetic field) over an interval centered on local midnight for stations equatorwards of 55° corrected geomagnetic latitude (CGML). The *IHV*-index is a close proxy for a single physical quantity, namely the power flux, *HP* [measured in GigaWatt], carried into the Earth's upper atmosphere by precipitating auroral charged particles. *HP* is routinely measured by NOAA/TIROS and DMSP satellites (since 1978). The *IHV* (and *HP*) index is proportional to the product of the cube-root of the solar wind momentum flux, $(nV^2)^{1/3}$, intercepted by the magnetosphere and to the flux of reconnected solar wind magnetic fields, *BV*. For longer-term averages, the dependency simplifies to $IHV \sim BV^2$. The *IHV*-index for a given station stands on its own, but for construction of a global index can be corrected for UT-effects and station location and normalized to the NGK station. The *IHV*-index has, so far, been derived back to 1844, with further extension and cross-checking possible, once existing 19-century observatory yearbook data become electronically available.

2) The Inter-Day-Variability (*IDV*-) index is defined as the unsigned difference between the hourly means for two successive days (of the H-component of the geomagnetic field) for the hour following local midnight for stations equatorwards of 51° CGML. The *IDV*-index is a proxy for the energy content of the ring current which in turn is controlled by the open flux in the magnetotail, ultimately depending on IMF *B*. The negative part of the *Dst*-index (or *Dst* derived from night-time data only) is, if one includes the ~25 nT 'quiet-time' component, simply proportional to *B*. The *IDV*-index for a given station stands on its own, but for construction of a global index can be corrected for station location and normalized to NGK. The *IDV*-index is a modern version of Bartels' classical *u*-measure and is available back to 1872 with further extension possible.

3) The solar wind electric field, $-V \times B$, maps down to an electric potential across the Earth's polar caps giving rise to an ionospheric Hall current that is directed towards the sun as the Earth turns under it. The magnetic effect of this current has been measured (with some early data gaps, of course) back to the First Polar Year (1882) and can be calibrated with modern data to allow determination of the product BV .

Collectively, these three indices give us an over-determined system for extracting the long-term variation over the past ~ 130 years of B and V . The analysis so far indicates that the variation of B can be described as a constant value (4.5 nT) plus a component varying with the square-root of the sunspot number. Because the latter seems to exhibit a ~ 100 year Gleissberg cycle, B does as well. The solar wind speed, V , seems to have increased linearly by 15% over the last 130 years and thus not to follow the Gleissberg cycle.

The IHV -index fords a way to check to calibration of other long-term geomagnetic indices. We find that the ap -index tracks the variation of IHV , but that the aa -index is systematically too low (3-5 nT) before 1957.

1. Geomagnetic Activity Indices

A Geomagnetic Index aims to be a summary of certain aspects of the very complicated phenomenon of geomagnetic activity. Ideally, a given geomagnetic index should:

1. Monitor a single class of geomagnetic variations stemming from a definite physical cause. In reality, complex phenomena have several simultaneous, interacting, and hard to separate causes, so we have to accept the concept of a class of related or co-operating causes being monitored.
2. Be simple to derive without requiring elaborate empirical conversion tables or model-dependent fitting procedures.
3. Be reproducible by automatic means using available observational data.

When it was discovered (long ago) that the geomagnetic field measured at a point on the Earth's surface not only had a secular variation but also varied slightly on time scales from seconds to years, it was also noted that these variations showed a "regular irregularity and irregular regularity" that frustrated interpretation and explanation. Even today, we do not know for sure the causes of some of the "regular" variations, *e.g.* the semiannual/universal time variation and the annual variation.

1.1. Geomagnetic activity is caused by solar wind interaction

Today we would characterize geomagnetic activity as those variations that result from the interaction between the solar wind and the magnetosphere:

1. Compression and confinement of the Earth's magnetic field, and
2. Transferring flux to the magnetotail by magnetic reconnection.

When (and afterwards) the stressed magnetosphere gives way and relaxes to a lower energy state, induced electric currents flow. Their magnetic effects we call geomagnetic activity and we try to characterize the phenomenon by indices.

1.2. Physical inputs to the system

These are thus the physical "inputs" to the system:

1. The interplanetary magnetic (B) flux per unit time and area, $F = B V$
2. The solar wind momentum ($n V$) flux per unit time and area, $P = (n V) V$

3. The angles between the Earth's magnetic field and the IMF direction (α) and flow direction (ψ)
4. The time scale of interest (hours to days) and the variability within that

2. Analysis of the *am*-index

We'll start with an analysis of a well-established activity index: the *am*-index defined by Mayaud (1967, 1968), and then transition to our own *IHV*-index (Svalgaard et al. 2003; Svalgaard et al., 2004) covering a much longer time interval.

A common technique in laboratory physics is to keep all variables nearly constant except one and investigate the effect of varying only that one. We can simulate this approach by selecting subsets of the vast dataset available (<http://omniweb.gsfc.nasa.gov>). The difference in time resolution (1 hour for the solar wind data and 3 hours for the *am*-index) is matched by averaging the shorter time resolution into the longer one.

2.1. Dependence on IMF flux

We first vary only the IMF strength keeping V in a narrow interval (395 ± 55 km/s). Similarly, the density, n , is kept in the interval 5 ± 1 protons/cm³, and the variability (see below) in the interval 0.5 ± 0.1 . These values correspond to average solar wind conditions. The result is shown in Figure 1

[Figure 1]

The *am*-index seems to vary with the first power of B both for northward ($\cos \alpha > 0$) and for southward ($\cos \alpha < 0$) merging angles. Repeating the analysis for other (narrow) intervals of solar wind speed V gives essentially the same result. This suggests that we can eliminate the influence of BV by dividing *am* by BV . We shall often use the abbreviation V_0 for $V/100$ km/s. The ' \sim ' symbol in this paper means 'equal to within a constant (possibly including a small offset)' or 'approximately equal to', depending on context.

2.2. Dependence on momentum flux

Figure 2 shows how activity (reduced by BV_0) depends on the momentum flux, nV_0^2 . It appears we can eliminate the influence of the solar wind momentum flux by dividing by the cube-root of nV^2 :

$$am' = am (\langle BV \rangle / BV) (\langle nV^2 \rangle / nV^2)^{1/3}$$

where $\langle \dots \rangle$ denotes the average value.

[Figure 2]

2.3. Dependence on IMF variability

The *am*-index is a three-hour index and during that interval the IMF can vary significantly (mostly in direction). We express the variability of the IMF by the ratio

$$f = (\sigma_{BX}^2 + \sigma_{BY}^2 + \sigma_{BZ}^2)^{1/2} / B$$

The efficiency of the coupling between the solar wind and the magnetosphere depends on the merging angle α , but also critically on the variability, f . When $f = 1$, there is no real dependence on α as the field varies randomly within the time interval, but for $f = 0$, there is a strong effect of steady southward fields ($\cos \alpha < 0$) as shown in Figure 3a.

2.4. Dependence on merging angle

The coupling function of f and $\cos \alpha$ is shown in Figure 3b and can be modeled by an exponential

$$q(f, \cos \alpha) \sim \exp[-p_4(f, \cos \alpha)]$$

where the argument, p_4 , is a fourth-order polynomial fit to f and $\cos \alpha$.

[Figure 3a & b]

This relationship is, of course, purely empirical and aims only at a (as it turns out, fairly accurate) *description* of the dependence.

We can then write

$$am \sim BV (nV^2)^{1/3} q(f, \cos \alpha)$$

With this relationship we can now **calculate** the am -index values from solar wind parameters. Figures 4a and 4b show typical results for several 27-day Bartels rotations.

[Figure 4 a & b]

The analysis described above (Figure 4a) was actually carried out 30 years ago using the first solar cycle's worth of interplanetary data (Svalgaard, 1977). Our recent analysis of three additional cycles fully confirms the early results (Figure 4b). The Figures show computed and observed am -values for individual three-hour intervals through six Bartels rotations each. The scale is logarithmic to show that the fit is equally good for both high and low values, except for the very lowest values of am , which are not reliable as they are very difficult to measure. These low values are systematically measured to be too low by perhaps 5 nT. Adding 5 nT to am would fix this and not impact the fit for large values of am .

2.5. Physical basis for range indices

For averages over months or years, $\langle \cos \alpha \rangle$ is to first order constant, but $\langle f \rangle$ is not. At times with high solar wind speed, f is higher too, increasing the coupling efficiency. The net result is that the expression $am \sim Bn^{1/3}V^{5/3}$, that is valid for individual three-hour intervals, for longer-term averages acquires a slightly higher exponent for V , namely V^2 . Noting that longer-term averages of $n^{1/3}$ do not vary much, we finally end with the expectation that $am \sim BV^2$ for averages over months or more, and this is indeed what we find. There is thus a quantitative physical basis for the am -index (and other such range indices).

3. The *IHV*-index

A problem with the am -index is that it only goes back to 1959. Similar indices (ap and aa) go back further but have uncertain (or possibly wrong) calibrations and cannot be reproduced. The main (actually the only) difficulty with these indices (or their equivalent K -indices) is the identification and removal of the (“irregularly” varying) regular diurnal variation. We attempt to sidestep this difficulty by only using data from the nighttime and define the Inter-Hour Variability index (*IHV*) as the sum of the six *unsigned* differences between hourly (mean) values of a geomagnetic element (for this paper we use the H-component) for the seven-hour interval centered on local midnight, the fourth hour containing midnight. Certain phenomena occur chiefly on the dayside of the magnetosphere (e.g. solar flare effects, the ‘regular’ solar quiet-time thermal wind and tidal effects, sudden storm commencements, the Svalgaard- Mansurov effect) and have physical causes distinct from the ‘classical’ geomagnetic activity that peaks near midnight.

The *IHV*-index can be automatically derived from ‘yearbook’ data, which go back to the 1840s. There is a technical matter having to do with the difference between hourly values (instantaneous on the hour mark) and hourly means (mean values over an hour usually centered on the half-hour mark). The latter were introduced by A. Schmidt with the 1905 Potsdam yearbook. Mean values have lower variance and thus lower *IHV*-values. This effect can reach 60%, but can easily be corrected for, once identified in the data.

3.1. Nighttime interval used for *IHV*

Figure 5 shows a sequence of magnetograms from Fredericksburg (FRD, U.S.A.). The red boxes outline the intervals used for calculation of *IHV*. The Figure illustrates the regular daily variation and its variability from day to day.

[Figure 5]

Figure 6 shows monthly means of *IHV* for FRD (blue) compared to monthly means of simultaneous *am* values (thick red curve). The thin pink curve is simply $0.7475 \text{ } IHV$ and matches the *am*-curve well, suggesting the use of *IHV* as a proxy for *am*.

[Figure 6]

3.2. Latitude dependence of *IHV*

IHV is a *subauroral* zone index (less than 55° corrected geomagnetic latitude) just like *am*. Figure 7 shows the average *IHV* for all stations (128 of them) with data in the WDCs during 1996-2003 as a function of corrected geomagnetic latitude. Note the dramatic increase for stations above 55° . Closer analysis also shows that high-latitude *IHV* reacts differently to solar wind parameters. It is therefore important to limit the application of *IHV* to subauroral stations.

[Figure 7]

3.3. Constructing a global *IHV*-index

We saw that even a single station is enough to obtain a reliable *IHV* proxy for *am*. To get a global index, we divide the globe into six longitude sectors with each a northern and southern latitude part and combine available stations (normalized to Niemegek, NGK) into an index for each sector. Figure 8 shows Bartels rotation averages for the European sector during years 1960-1971 illustrating the consistency of the index values from station to station.

[Figure 8]

Averaging all sectors gives us a global composite *IHV*-index covering all Universal times and both hemispheres.

3.4. Correlation of *IHV* with solar wind parameters

Because the *am*-index varies with BV^2 , we expect *IHV* to do the same, and so it does, as shown in Figure 9a and 9b. We had turned the correlations around calculating solar wind parameters from geomagnetic activity instead of activity from solar wind parameters. This allows us to estimate solar wind and interplanetary physical quantities using the Earth’s magnetosphere as the measuring device.

[Figure 9a & b]

There are a couple of areas of less agreement (marked with circles). We actually understand the reason for these. There is a 22-year cycle (Russell, 1974) in geomagnetic activity partly caused by a combination of two effects. The Russell-McPherron effect causes opposite annual variations of southward IMF for the two polarities of the IMF (Russell and McPherron, 1973). During the minimum and rising phases of the solar cycle there is an imbalance between the occurrence of the two polarities (the Rosenberg-Coleman effect, Rosenberg and Coleman, 1969). Because the solar polar fields show a 22-year cycle, the combination of these two effects results in geomagnetic activity being higher every other cycle when the R-C effect is present. The green line shows the size of the R-C effect (in arbitrary units) derived from the observed IMF polarity (Echer and Svalgaard, 2004). We leave these second-order discrepancies in the *IHV*-index with the knowledge that they exist.

3.5. Eliminating dipole-tilt modulation

Both *am* and (raw) *IHV* show a dependence on the tilt angle of the Earth's dipole towards the solar wind direction (ψ): $am \sim S(\psi) = (1+3 \cos^2\psi)^{-2/3}$ as shown in Figures 10a and 10b (Svalgaard, 1977; Svalgaard et al, 2002; O'Brien and McPherron, 2004, McPherron, 2004). Since the dipole axis is inclined 11° to the rotation axis, this dependence, involving the dipole field strength at the subsolar point, introduces an undesirable dependence on longitude. We eliminate this by dividing *IHV* by the function $S(\psi)$. In this way, *IHV*-values from stations at different longitudes can be directly combined. The ψ -dependence is a true **modulation** of existing activity. It does not depend on the direction of the IMF (Northwards or Southwards fields).

[Figure 10a & b]

3.6. Hemispheric power input

As the stressed magnetosphere gives way, particles are accelerated and precipitate into the upper atmosphere over the polar regions where the energy thus deposited can be directly measured by polar-orbiting satellites (POES). From the satellite data (Figure 11a) the total energy input (in Gigawatt) to each hemisphere can be estimated (Foster et al., 1986; Emery et al., 2006). Such estimates exist back to 1978. It turns out that the *IHV*-index is proportional to the Hemispheric Power input, giving a direct physical interpretation of *IHV*. Figure 11b shows the correlation of rotation means of the hemispheric power input and the *IHV*-index.

[Figure 11a, b, & c]

Figure 11c shows a comparison between the observed and calculated power since the start of the satellite measurements. The close agreement validates the (semi-)empirical method used to estimate the hemispheric integrated power input from the discrete satellite pass measurements.

4. The *IDV*-index

The *IHV*-index captures activity on a time scale of hours. How about on a time scale of days or longer? Bartels defined his *u*-measure as the monthly (or longer) mean of the unsigned differences between the mean values of the H-component on two successive days. We found that you get essentially the same result using the mean over the whole day, a few hours, or only one hour. Our Interdiurnal Variability index (*IDV*) (Svalgaard and Cliver, 2005) is then simply a modern version of the *u*-measure (in nT, not the original 10 nT units; Bartels, 1932) using only one hour (preferably the midnight hour if available). Figure 12 shows how $10u$ and *IDV* match up. Note that *u* and *IDV* did not register the strong high-speed streams in 1930, 1952, 1974, 1994, and 2003. The failure to register the very high 1930 activity level was a deadly blow to the *u*-measure, causing Bartels to abandon the index.

[Figure 12]

4.1. IDV is a proxy for IMF B

What *is* the IDV -index then measuring? In Figure 13 we plot yearly averages of B and V against IDV : There is indeed no correlation with V . There *is* a robust correlation with B (with or without a few outliers - blue circles [Lockwood et al., 2006b]). Various fits (linear, power law) do not really differ over the range of the data (Svalgaard and Cliver, 2006a).

[Figure 13]

4.2. IDV and Dst measure the same thing

Coronal Mass Ejections (CMEs) add (closed) magnetic flux to the IMF and also compress the ambient IMF. The resulting strong magnetic fields of CMEs hitting the Earth create magnetic storms, feeding energy into the inner magnetosphere (“ring current”). The Dst -index is aimed at describing this same phenomenon, but only the negative contribution to Dst on the nightside is effectively involved. Because positive and negative values of Dst are due to different physical processes (controlled roughly by solar wind pressure and magnetic reconnection, respectively) a simple yearly average of Dst is a somewhat suspect physical quantity. If we include only negative values of Dst in the average, the correlation we isolate the effects of magnetic reconnection. We therefore expect (negative) Dst and IDV to be strongly related, and they are as shown in Figure 14a.

[Figure 14a & b]

We used a derivation of Dst by J. Love back to 1905 (Love, 2006). Similar results are obtained with the Dst series by Karinen and Mursula (2005) back to 1932 or with the “official” Dst series, back to 1957. The very simple-to-derive IDV series compares favorably with the more elaborate $Dst(< 0)$ as seen in Figure 14b showing both time series (IDV and IDV calculated from $Dst(< 0)$).

Using regressions of IDV and $Dst(< 0)$ on IMF B we can directly estimate B back to 1872 with the result shown in Figure 15: There is a hint of a ≈ 100 -year Gleissberg-type cycle.

[Figure 15]

4.3. Very long-term variation of IDV (and B)

Can we go further back in time? Bartels had determined the u -measure from 1836 on, but with less confidence before 1872. Figure 16 shows what we get if we infer IDV (and then B) from u back to 1836.

[Figure 16]

The smooth curve is a 4th-order polynomial fit. One can also just fit the values at solar minima (to eliminate most solar activity) with essentially the same result. We may be approaching another minimum in the Gleissberg cycle. The IMF B for 2006 (so far, through September) is the lowest in the last 94 years.

The main sources of the equatorial components of the Sun’s large-scale magnetic field are large active regions. If these active regions emerge at random longitudes, their net equatorial dipole moment will scale as the square root of their number. Thus their contribution to the average IMF strength will tend to increase as the square root of sunspot number, Rz , (for a detailed discussion, see Wang and Sheeley, 2003). There is, indeed, such a correlation (Figure 17a; Svalgaard and Cliver, 2005), and we can therefore attempt to infer B from Rz as well and compare with B inferred from u (Figure 17b). Before about 1850, either u is too large or Rz is too small. This is problem for further research.

[Figure 17a &b]

5. The Polar Cap Potential index

Across the Earth's polar caps flows a current in the ionosphere (Ritter et al., 2004). This is a Hall current basically flowing towards the sun (Figure 18). The Earth rotates under this current causing the magnetic effect of the current to rotate once in 24 hours adding a circular motion to the end-point of the horizontal component vector. This rotating daily effect is readily (and has been since 1882, Figure 19a) observed at polar cap magnetic observatories (Figure 19b). The current derives from the Polar Cap Electric Potential which is basically the electric field ($\mathbf{E} = -\mathbf{V} \times \mathbf{B}$) in the solar wind mapped down to the ionosphere.

[Figure 18]

[Figure 19a & b]

5.1. Dependence on solar wind electric field

Figure 20a shows for each year of 1965-2004 how the average radius of the circular variation of the end-point of the horizontal component depends on the product of B and V for Thule (THL) and for Resolute Bay (RES). The radius of the circular variation is virtually the same for all stations in the cap. The radius of the circle traced out by variation of horizontal component is a measure of the polar cap potential. For stations near the polar cap boundary the circle is only partial. We can then estimate the time variation of BV as shown in Figure 20b.

[Figure 20a & b]

6. Determining solar wind parameters from the indices

We now have three independent ways of estimating solar wind and IMF parameters:

1. The IHV -index, estimating BV^2
2. The IDV -index, estimating B
3. Polar Cap Potential index, estimating BV

These indices are readily computed from simple hourly means (or values) for which we have measurements stretching back well into the 19th century.

We can thus estimate $V = \sqrt{[(BV^2) / B]}$ and use that value to calculate BV for comparison with the estimated BV . The agreement (Figure 21) is encouraging. There are several second-order effects (22-year cycle, solar cycle variations of ionospheric conductivity, secular decrease of Earth's dipole moment, records going off-scale, etc) that can be compensated for, but the overall picture seems clear already.

[Figure 21]

6.1. Cross-checking the aa -index

We can even use the IHV -index as a check on the long-term stability of the aa -index (Mayaud, 1972). Regressing aa versus IHV for recent times we find excellent agreement (Figure 22).

[Figure 22]

Using the regression of Figure 22 we can calculate aa under the assumption that the aa -index has a calibration that is constant in time (Figure 23). Figure 24 shows the difference between observed and calculated

Bartels rotation averages of the *aa*-index since 1890. Note the marked discontinuity at the beginning of the year 1957. It would seem that the *aa*-index is in need of a recalibration. The same conclusion was also reached by Svalgaard et al (2004), Jarvis (2005), Svalgaard and Cliver (2006b), and Lockwood et al. (2006a)

[Figure 23]

[Figure 24]

6.2. Geomagnetic activity back to 1844

The analyses and results presented in this review paper underscore the immense value of old geomagnetic records. An effort should be made to preserve that legacy and to bring the data into electronic form. We can then apply the same technique for that early data. Figure 25 shows the result of using the Helsinki observatory data (1844-1897) to extend *IHV* (converted to *aa* using the regression of Figure 22) back to 1844. For comparison we also plot (Figure 26) the *ak*-index derived from the same data by Nevanlinna and Kataja (1993). As the *ak*-index was normalized to match the *aa*-index for the time when they overlap it is not surprising that *ak* is also lower than our *IHV* converted to *aa*. The simplicity and reproducibility of *IHV* compared to *aa* and similar indices might inspire confidence in the long-term calibration of this objective measure of geomagnetic activity.

[Figure 25]

7. Conclusion

By constructing geomagnetic indices that are directly related to separate physical conditions in Geospace we bring investigations of the long-term behavior of these conditions onto a firm physical basis and remove much of the speculative character of our inferences about Space Climate. At the same time we are able to bring the historical record of geomagnetic measurements to bear on the issues of Space Climate in ways our predecessors could not dream of, but would certainly much appreciate and delight in.

References

- Bartels, J. Terrestrial-magnetic activity and its relations to solar phenomena, *Terr. Magn. Atmos. Elec.* 37, 1., 1932.
- Echer, E., Svalgaard, L. Asymmetry in the Rosenberg-Coleman effect around solar minimum revealed by wavelet analysis of the interplanetary magnetic field polarity data (1927-2002), *Geophys. Res. Lett.* 31(12), L12808, doi:10.1029/2004GL020228, 2004.
- Emery, B., A., Evans, D. S., Rich, F. J., Xu, W. Low energy auroral ion and electron hemispheric power variations with activity indices (submitted) *J. Geophys. Res.*, 2006.
- Foster, J. C., Holt, J. M., Musgrove, R. G., Evans, D. S. Ionospheric convection associated with discrete levels of particle precipitation, *Geophys. Res. Lett.* 13, 656-659, 1986.
- Jarvis, M. (2005), Observed tidal variation in the lower thermosphere through the 20th century and the possible implication of ozone depletion, *J. Geophys. Res.*, 110, A04303, doi:10.1029/2004JA010921.
- Karinen, A., Mursula, K. A new reconstruction of the Dst index for 1932-2002, *Ann. Geophys.* 23(2), 475-485, 2005.
- Lockwood, M., Whiter, D., Hancock, B., Henwood, R., Ulich, T., Linthe, H. J., Clarke, E., Clilverd, M. A. The long-term drift in geomagnetic activity: Calibration of the *aa* index using data from a variety of magnetometer stations, *Ann. Geophys.*, in press, 2006a.

Lockwood M., Rouillard, A. P., Finch, I., Stamper, R. Comment on “The IDV index: Its derivation and use in inferring long-term variations of the interplanetary magnetic field strength” by Leif Svalgaard and Edward W. Cliver, *J. Geophys. Res.*, 111, A09109, doi:10.1029/2006JA011640, 2006b.

Love, J. Personal Communication, 2006.

Mayaud, P. N. Calcul préliminaire d'indices Km, Kn et Ks ou Am, An, et As, mesures de l'activité magnétique à l'échelle mondiale et dans les hémisphères Nord et Sud, *Ann. Géophys.* 23, 585, 1967.

Mayaud, P. N. Indices Kn, Ks, et Km, 1964-67, Centre National de la Recherche Scientifique, Paris, 1968.

Mayaud, P. N. The aa index: a 100-year series characterizing the geomagnetic activity, *J. Geophys. Res.* 77, 6870, 1972

McPherron, R. L. Energy Input to the Magnetosphere and its Dissipation in the Ionosphere, American Geophysical Union, Fall Meeting 2004, abstract #SA13B-03, 2004.

Nevanlinna, H., Kataja, E. An extension of the geomagnetic activity index series aa for two solar cycles (1844-1868), *Geophys. Res. Lett.* 20(23), 2703-2706, 1993.

O'Brien, T. P., McPherron, R. L. Seasonal and diurnal variation of Dst dynamics, *J. Geophys. Res.* 107(A11), 1341, doi: 10.1029/2002JA009435, 2002.

Rosenberg, R. L., Coleman, P. J. Heliographic latitude dependence of dominant polarity of interplanetary magnetic field, *J. Geophys. Res.* 74, 5611, 1969.

Ritter, P., Lühr, H., Viljanen, A., Amm, O., Pulkkinen, A., Sillanpää, I. Ionospheric currents estimated simultaneously from CHAMP satellite and IMAGE ground-based magnetic field measurements: a statistical study at auroral latitudes, *Ann. Geophys.* 22(2), 417-430, 2004.

Russell, C. T. On the heliographic latitude dependence of the interplanetary magnetic field as deduced from the 22-year cycle of geomagnetic activity, *Geophys. Res. Lett.* 1, 11, 1974.

Russell, C. T., McPherron, R. L. Semiannual variation of geomagnetic activity, *J. Geophys. Res.* 78, 92, 1973.

Svalgaard, L., Geomagnetic activity: Dependence on solar wind parameters, in *Coronal Holes and High Speed Wind Streams*, ed. J. B. Zirker, 371, Colorado Associated University Press, Boulder, CO, 1977.

Svalgaard, L., Cliver, E. W., Ling, A. G. The semiannual variation of great geomagnetic storms, *Geophys. Res. Lett.* 29(16), 12, citeID 1765, doi 10.1029/2001GL014145, 2002.

Svalgaard, L., Cliver, E. W., Le Sager, P. Determination of interplanetary magnetic field strength, solar wind speed and EUV irradiance, 1890–2003, in *Solar Variability as an Input to the Earth's Environment*, ISCS Symp., p. 15, Eur. Space Agency, Paris, 2003.

Svalgaard, L., Cliver, E. W., Le Sager, P. IHV: A new long-term geomagnetic index, *Adv. Space Res.* 34(2), 436, 2004.

Svalgaard, L., Cliver, E. W. The IDV index: Its derivation and use in inferring long-term variations of the interplanetary magnetic field strength, *J. Geophys. Res.* 110, A12103, doi:10.1029/2005JA011203, 2005.

Svalgaard L., Cliver, E. W. Reply to the comment by M. Lockwood et al. on “The IDV index: Its derivation and use in inferring long-term variations of the interplanetary magnetic field”, J. Geophys. Res. 111, A09110, doi:10.1029/2006JA011678, 2006a.

Svalgaard, L., Cliver, E. W., Long-term variation of geomagnetic activity (the IHV-index) and its use in deriving solar wind speed since 1882, manuscript in preparation, 2006b.

Wang, Y.-M., Sheeley, N. R., Jr. On the fluctuating component of the Sun's large-scale magnetic field, Ap. J. 590(2), 1111, doi: 10.1086/375026, 2003.

Several of the papers cited and further work in progress may be found at <http://www.leif.org/research>.

Figure Captions

Figure 1: The dependence of the am -index on the field strength, B , of the interplanetary magnetic field (IMF) for almost constant values of all the other solar wind parameters. Filled circles represent cases where the IMF was largely southwards with respect to the geomagnetic field (i.e. $\cos \alpha < -0.25$); open circles represent cases of predominantly northwards field ($\cos \alpha > +0.25$), while circles with a dot represent cases of IMF largely perpendicular to the geomagnetic dipole. A typical error bar is shown in the center of the figure (after Svalgaard, 1977).

Figure 2: The dependence on the reduced (for BV) am -index on the solar wind momentum flux, nV_o^2 . A power law with exponent $1/3$ is an excellent fit to the data for 1963-1973 (after Svalgaard, 1977).

Figure 3: (a, top) The dependence of geomagnetic activity (am -index reduced for BV and nV_o^2 , see text) on $\cos \alpha$, where α is the angle between the geomagnetic field lines at the ‘nose’ of the magnetosphere and the average IMF direction during the three-hour interval corresponding to the am -range. Several curves are shown for various values of the relative variability f , from $f = 0.0$ to $f = 0.9$ as labeled on the Figure. Note the very flat curves for high variability and the steep curves for low variability of the IMF direction. (b, bottom) Bins of $\cos \alpha$ (0.1 wide) and bins of f (0.1 wide) were formed and the average value of reduced am was computed for each 2D bin. Contour levels less than average are shown as dashed lines (after Svalgaard, 1977).

Figure 4: (a) Observed and reconstructed am -indices for Bartels rotations 1836-1841 (Oct. 3, 1967 through March 12, 1968). For every three-hour interval where solar wind data was available, am was computed using the relationships deduced from the analysis quoted in this paper. The scale of am is logarithmic because we want to verify the synthesized am -indices against observations over the full range of the index. The two overlapping curves show the two indices for times when solar wind data was available. Where only a single curve is visible over a certain time interval it just means that the computed and the observed indices track each other perfectly. The main area of disagreement is for very small am -values (e.g. for $am \leq 1$; all such cases are plotted as $am = 1$). (b) As for Figure 4a, except for Bartels rotations 2250-2255 (May 11, 1998 through Oct. 19, 1998). The reconstructed index is shown in red. The best-fit fourth-order polynomial is given at the bottom of the Figure.

Figure 5: Sample magnetograms from Fredericksburg (FRD) showing the regular daily variation and *its* day-to-day variability. The boxes show the interval of each day where the regular variation is minimal: the local night hours. The three components (H - horizontal force, D - its direction, and Z - the vertical force) can all be used to construct geomagnetic indices, although the Z-component is especially prone to local induction effects and is therefore usually not used.

Figure 6: Monthly averages of the IHV -index calculated for FRD (blue curve) compared to the monthly average am -index (for the same two three-hour intervals that were used for FRD) (red curve). A simple scaling (pink) of the FRD-curve makes it a very close match to the am -curve, showing that IHV from even a single station can be used as a proxy for am .

Figure 7: Variation of IHV with corrected geomagnetic latitude. Average IHV over the interval 1996-2003 for each station with data in that interval are plotted. A few “outliers” are shown with small circles. Local induction effects may be responsible for these stations having about 25% higher IHV . The red curve shows a model fit to the larger circles.

Figure 8: Bartels rotation means of IHV for longitude sector 15° (Northern Hemisphere) for the years 1960-1971. IHV averaged over all stations in the sector is shown as a thick grey curve in the background and each station’s contribution is shown as a thin black curve. The IAGA codes for contributing stations are shown at the bottom of each plot.

Figure 9: (a) Relationship between Bartels rotation means of BV_o^2 and composite IHV for the interval 1965-2005. (b) Comparison of computed (blue) and observed BV_o^2 (red) running 13-rotation means. Areas of consistent disagreement are marked by ovals. These occur every other solar cycle when the Rosenberg-Coleman effect is large (amplitude on arbitrary scale given by green curve).

Figure 10: Variation of the S -function (c) and of “raw” IHV (a) with month of year and Universal Time calculated for *all* the 128 stations with data available during 1996-2003. The IHV values for a given station were assigned to the Universal Time of local midnight for that station. All values were divided by the average values for each station. The color coding over the $\sim 40\%$ variation is chosen such that purple, to red represents low to high values. (b) The seasonal and UT variation for the am index (From Svalgaard et al., 2002).

Figure 11: (a) Estimated hemispheric power estimates are computed for each POES satellite pass over the polar regions as data arrive at the Space Environment Center from the satellite tracking stations. Once the power input (in Gigawatt) is estimated, the corresponding statistical pattern of auroral power input is selected. Using the Universal Time of the satellite pass, the magnetic latitude and magnetic local time coordinates of the statistical pattern are converted to geographic coordinates; the pattern is then superimposed upon a geographic polar map of either the northern or southern hemisphere (<http://sec.noaa.gov/pmap/BackgroundInfo.html>). The Figure shows a typical result. (b) Relationship between the hemisphere power input for the Northern Hemisphere and the IHV for the same for the interval 1978-2006 showing a scaling factor of 0.68 to convert IHV to GW. (c) Comparison between the estimated POES hemispheric power input to the Northern Hemisphere (red) and the scaled IHV -index (blue) for the entire dataset set 1978-2006.

Figure 12: 10 times the u -measure (blue curve) for 1872-1936 compared to the IDV -index (red curve, derived as described in the text) for 1890-2004). For the time of overlap, the linear cross correlation coefficient is 0.95. Yearly averages of both indices are plotted.

Figure 13: Scatter-plot of yearly average IDV and the strength of the total interplanetary magnetic field, B (for all points [circles], and excluding a few outliers [small circles]), and the solar wind speed, V (triangles) for each year of the interval 1965-2006. The two regression lines for B as a function of IDV give very nearly the same result within the range of the observed data points. There is no correlation (square of linear cross correlation R^2 effectively zero) between IDV and V .

Figure 14: (a) Relationship between yearly averages of IDV and Dst using only negative Dst -values for the interval 1905-2004. Dst data courtesy of J. Love (2006). (b) IDV scaled from Dst (red curve) and observed (blue curve). Note the large discrepancy in 1909 where all stations used for IDV had missing data during the powerful September 1909 storm.

Figure 15: The magnitude B of the interplanetary magnetic field near the earth observed by spacecraft (red curve) and inferred from the IDV -index (blue curve and regression formula). The green curve shows B calculated from an extension (Love, 2006) back to 1905 of the Dst -index computed using only the negative values.

Figure 16: IMF B inferred from IDV using the regression with outliers omitted. Fourth-order polynomials fitted to all data (red curve) and sunspot minima data (open circles) only (black curve) hint at a ~ 100 year cycle. The 11-year running mean (grey curve) still shows a weak solar cycle variation.

Figure 17: (a) Yearly means of B derived from u and IDV or observed by spacecraft regressed against the square root of the Zürich (International) sunspot number. (b) Variation of yearly averages since 1836 of IMF B inferred from Bartels' u -measure, the sunspot number, the IDV -index, and observed by spacecraft (red)

Figure 18: Model of a sheet of line currents at 110 km height in the ionosphere. The magnetic effects of the currents are observed by spacecraft above the current sheet and by ground-based stations below the sheet (after Ritter et al., 2004).

Figure 19: Because the current is fixed with respect to the sun, the earth rotates underneath the current and the magnetic effect is organized in Solar Local Time (not magnetic local time). This makes it meaningful to plot the effect in terms of its X (North) and Y (East) components (two sine curves 6 hours apart) or as a corresponding vector diagram showing the movements of the end point of the effect vector in Y-X coordinates tracing out a circular path. This has been known for a long time viz.: (a) Vector diagram from Kingua Fjord during the First Polar Year 1882-1883. (b) Rotation of end-point of the horizontal component vector 1980-2004 for several stations in the Arctic polar cap: Alert (ALE), Thule (THL), Resolute Bay (RES), Cambridge Bay (CBB), and Baker Lake (BLC). For stations (ALE, THL, RES) that are well inside the auroral oval, the path is a neat circle (ALE is slightly perturbed by local induction effects) whose radius (the amplitude of the effect) is constant across the polar cap. Stations (CBB, BLC, and GJH) that are only well inside the oval part of the time show an effect that follows the nominal circular path as long as they stay inside, but are perturbed by the dayside cusp currents when not in the polar cap.

Figure 20: (a) We express the polar cap potential in terms of the solar wind electric field $V \times B$ as the product of solar wind speed V and magnetic field B . Here we show the close relationship between yearly averages of VB calculated from spacecraft measurements over 1965-2004 and the amplitudes of the horizontal variation for THL and for RES (there is no real difference) determining the scale factor. (b) We can then scale the geomagnetic data and compare the result with in situ space observations over the interval 1965-2006.

Figure 21: (top) Near Earth IMF strength B inferred from IDV (upper blue curve) and solar wind speed V_0 (lower blue curve) computed from IHV and B compared to in situ values observed by spacecraft (red curves). (bottom) Polar cap potential BV_0 calculated from the above values of B and V_0 compared to values scaled from the amplitude of the horizontal daily variation (green curve) and observed by spacecraft (red curve).

Figure 22: Relationship between Bartels rotation averages of the aa -index and the global IHV -index for the interval 1980-2004 where there were no (known) changes to the calibration of aa . The relationship is slightly non-linear, so a power-law was chosen as fitting function.

Figure 23: Comparison of fitted (blue) and observed (red) aa during 1990-2001. Note the 'wrap-around' in 1991. The fit is close to perfect.

Figure 24: Difference between observed and fitted aa during 1890-2006. After the beginning of 1957, the difference is close to zero, but before 1957, the observed aa -values are too low by 3-5 nT.

Figure 25: Using Helsinki (1844-1897), Wilhelmshafen (1883-1895), Batavia (1882-1894), Potsdam (1890-1907), Tokyo (1897-1912) and all available data from many stations since 1900 we can construct a composite IHV -series from the present back to 1844. This Figure shows Bartels rotation averages over the composite IHV -index overlain by (pink curve) the 13-rotation running mean.

Figure 26: Comparison between the ak -index (red) derived by Nevanlinna and Kataja (1993) and our IHV-index (blue) scaled to aa .

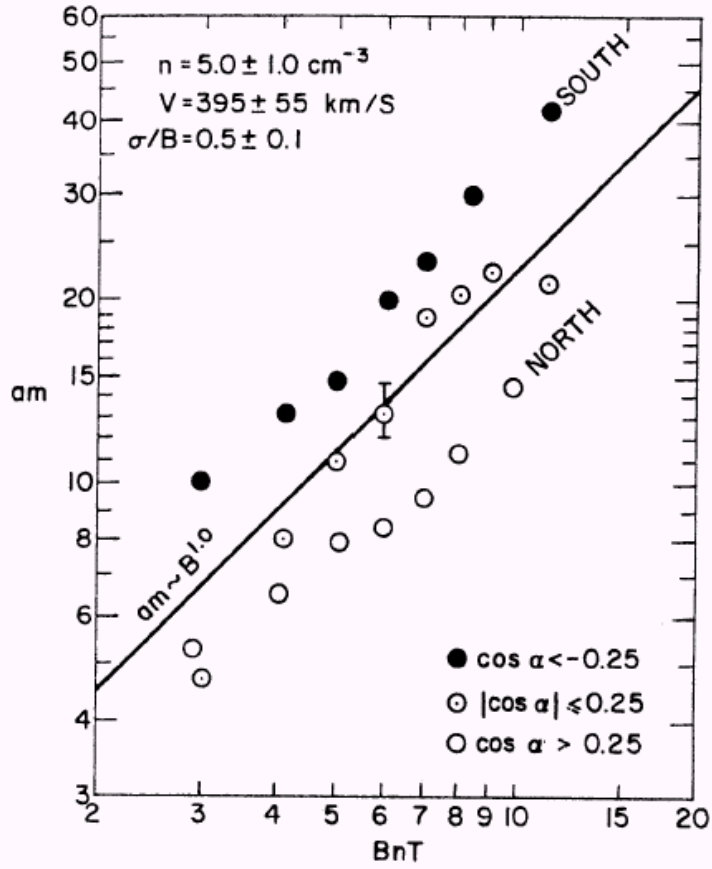


Figure 1

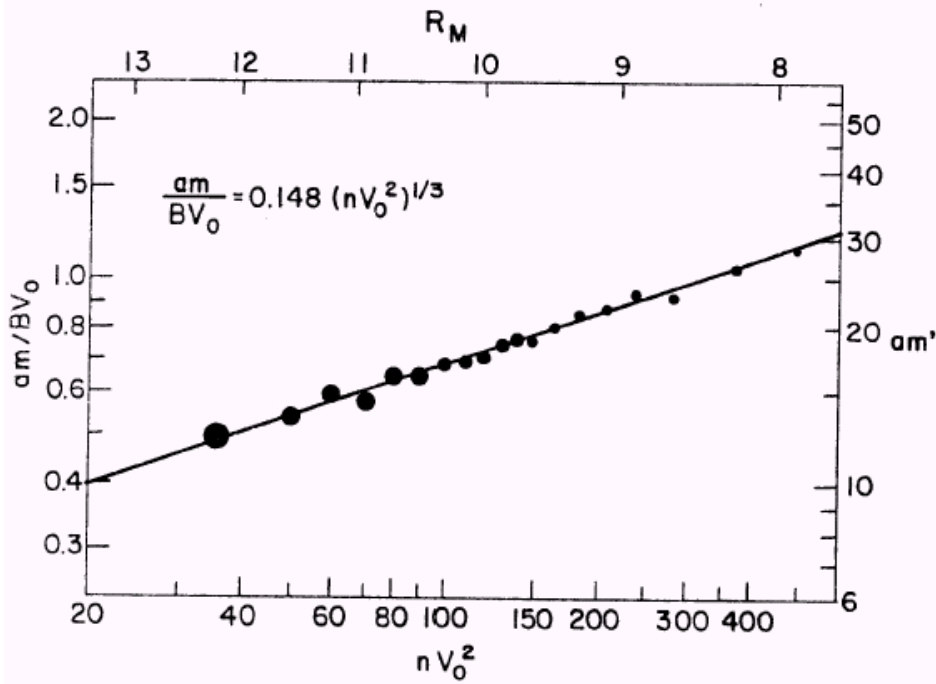


Figure 2

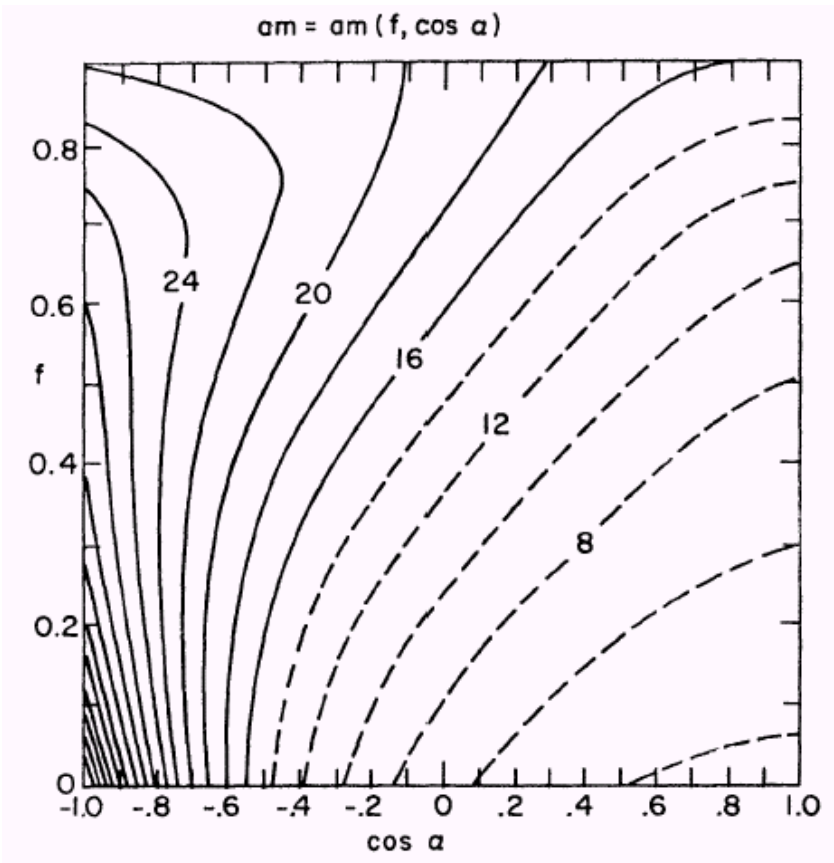
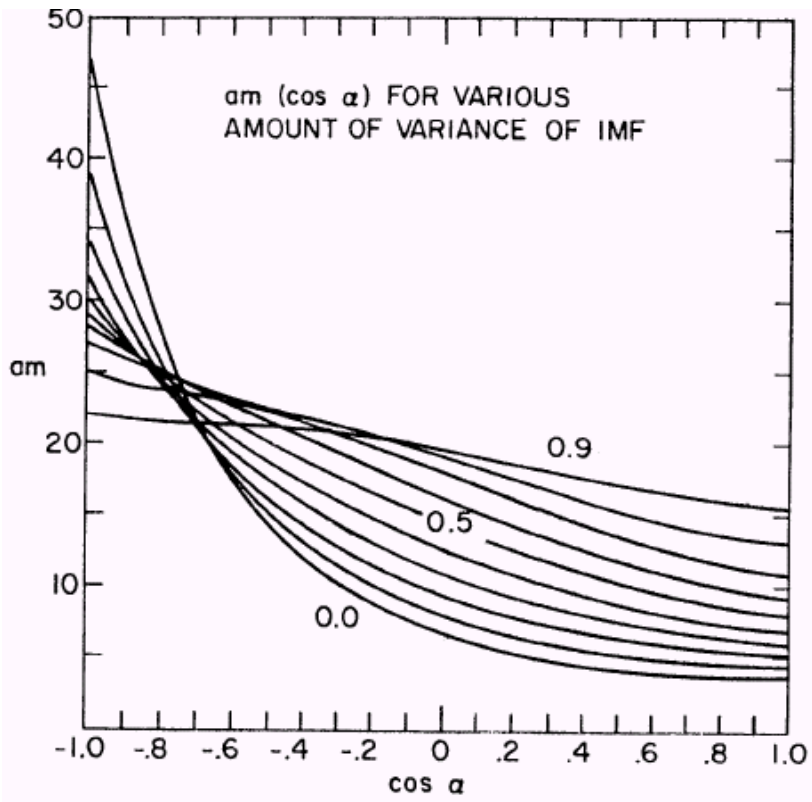


Figure 3 a (top) and 3b (bottom)

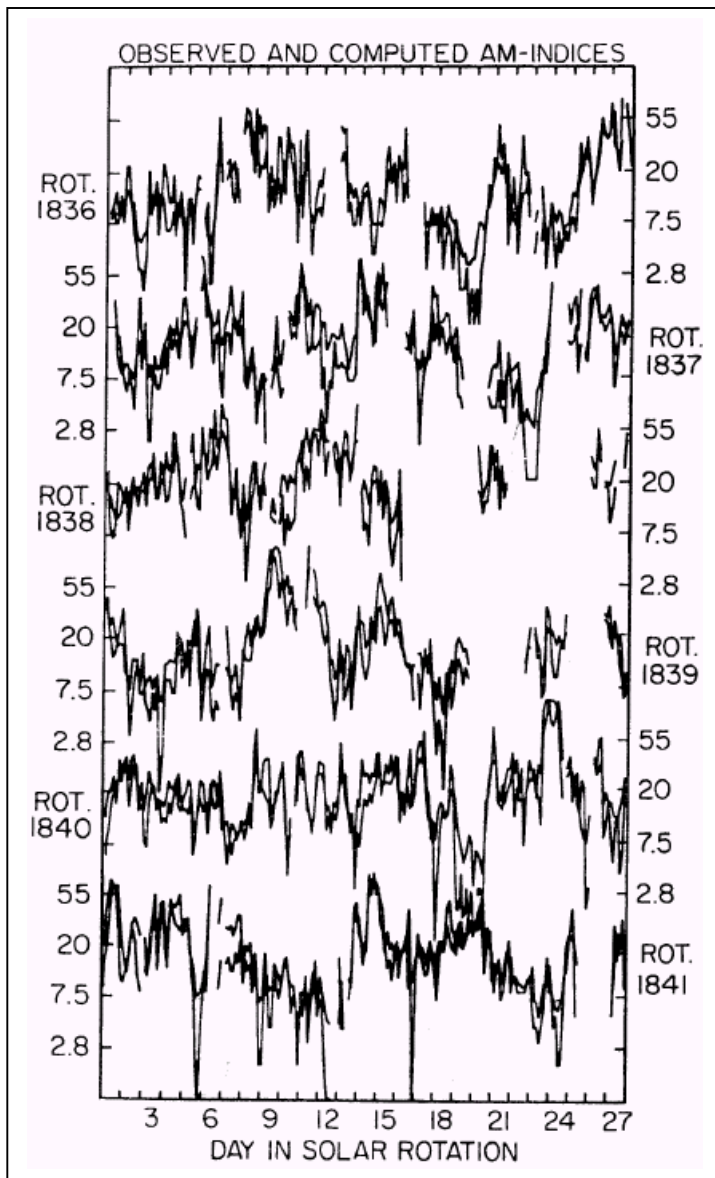


Figure 4a

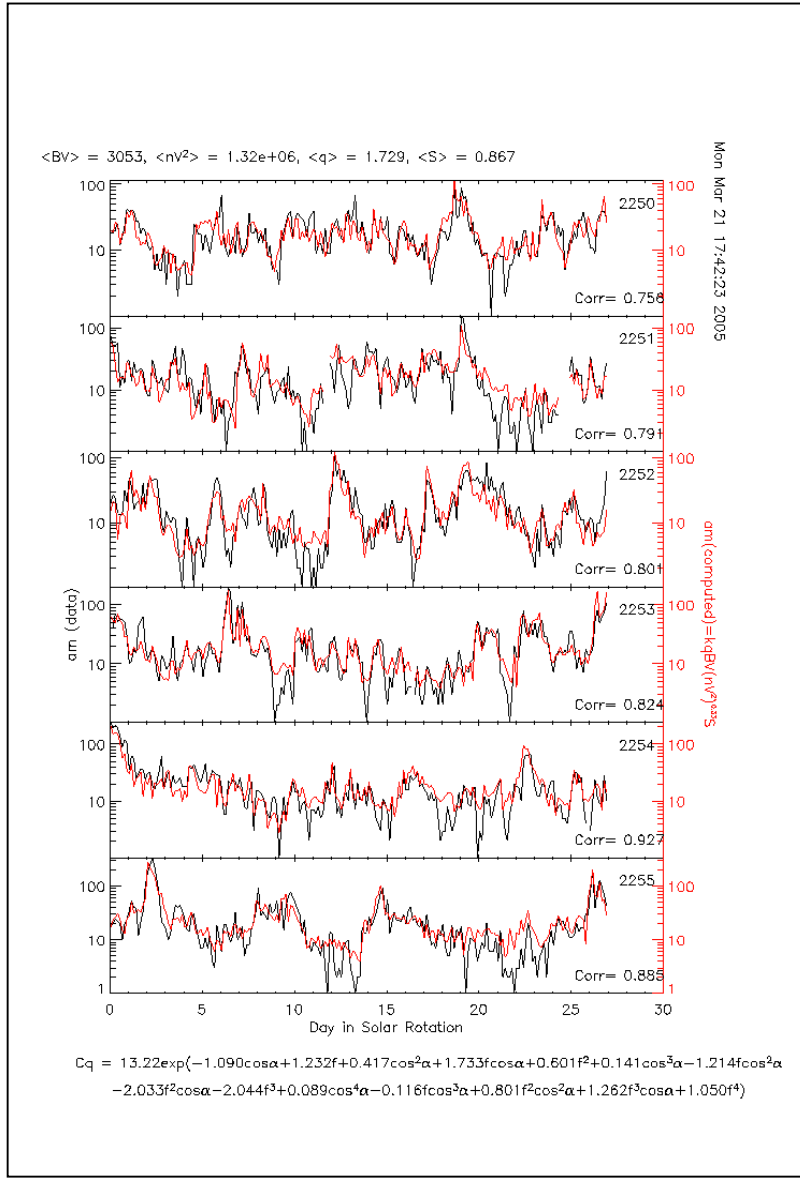


Figure 4b

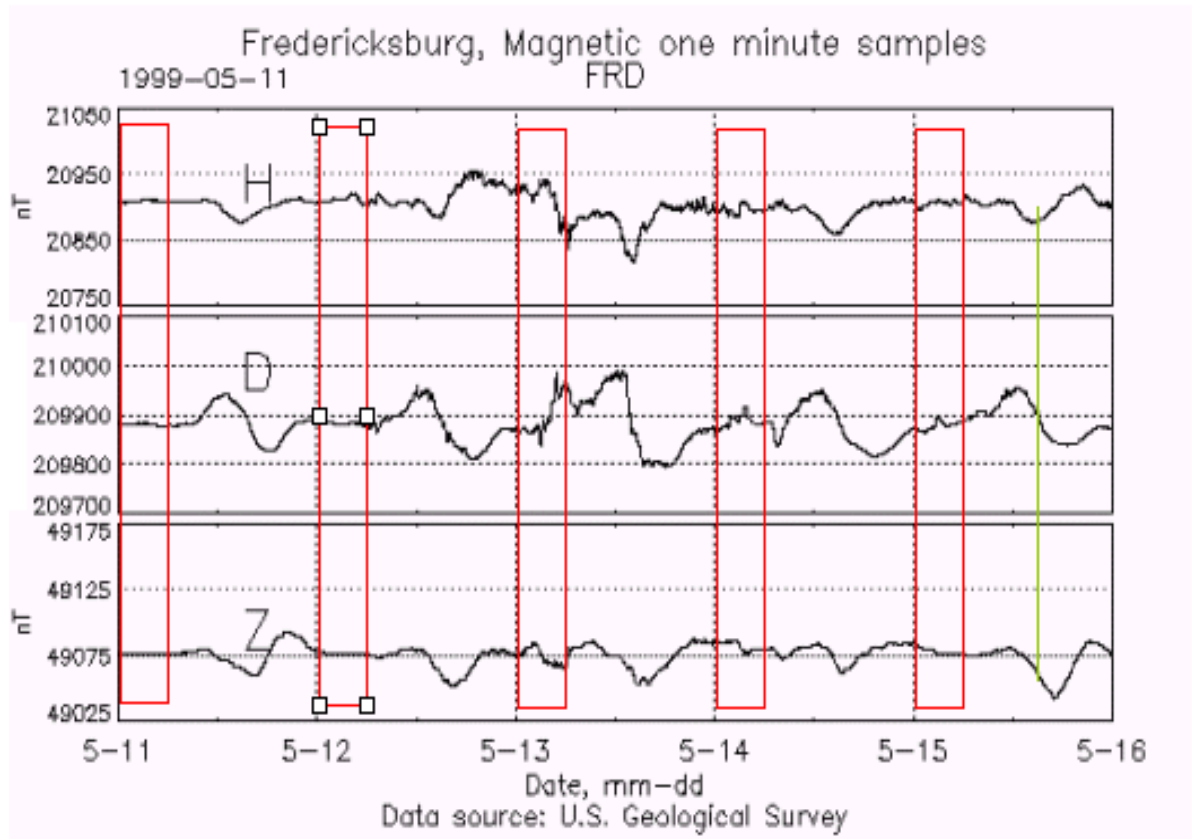


Figure 5

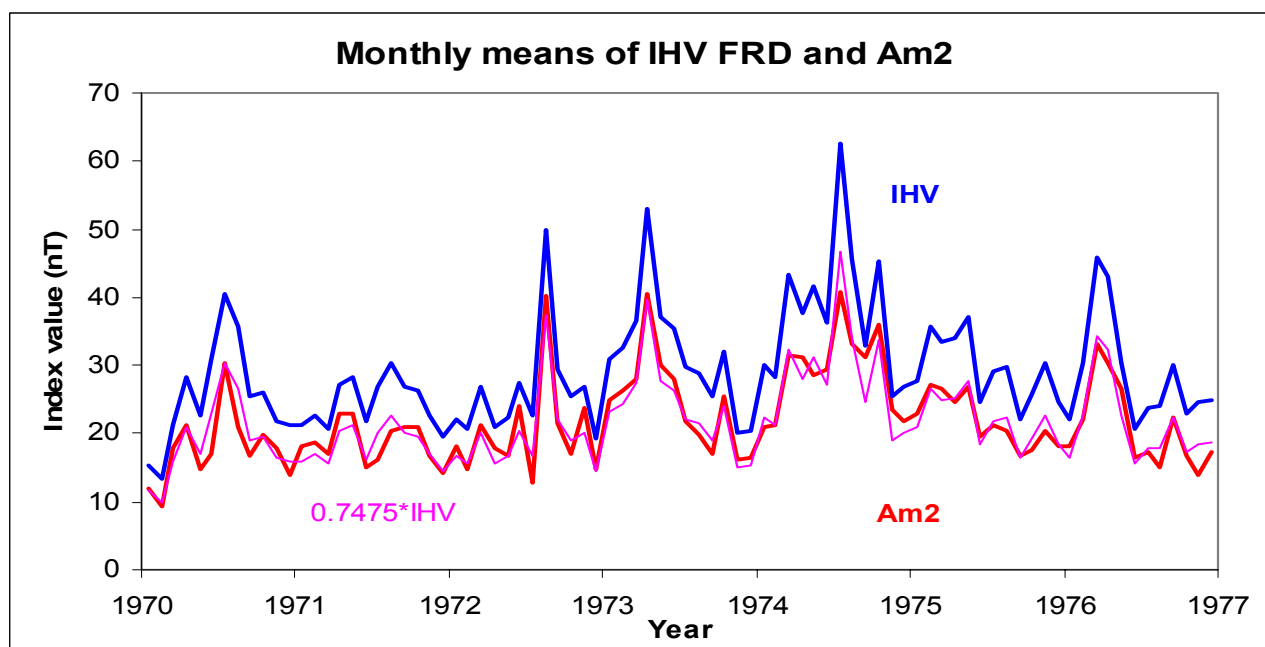


Figure 6

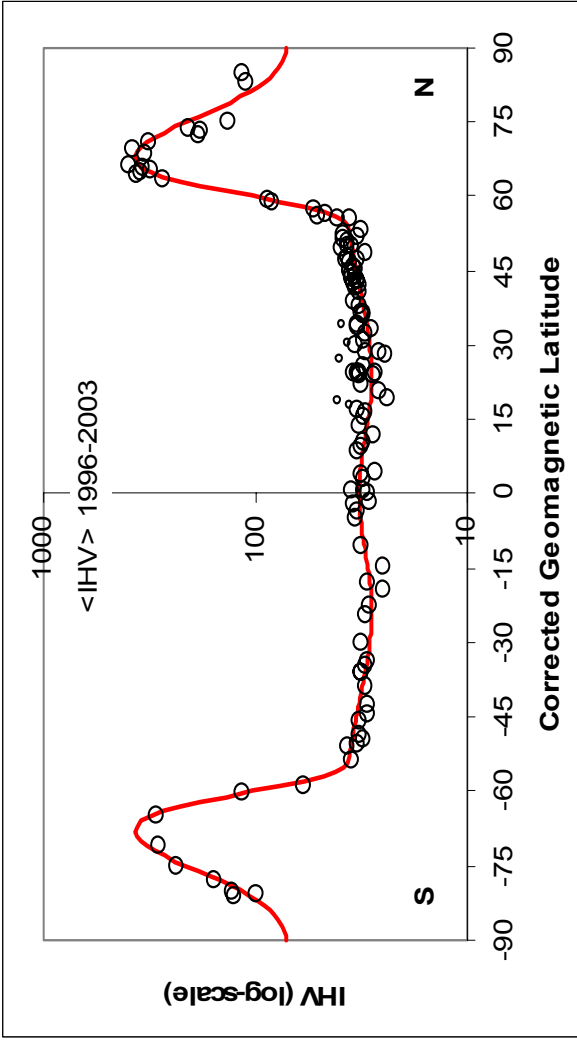


Figure 7

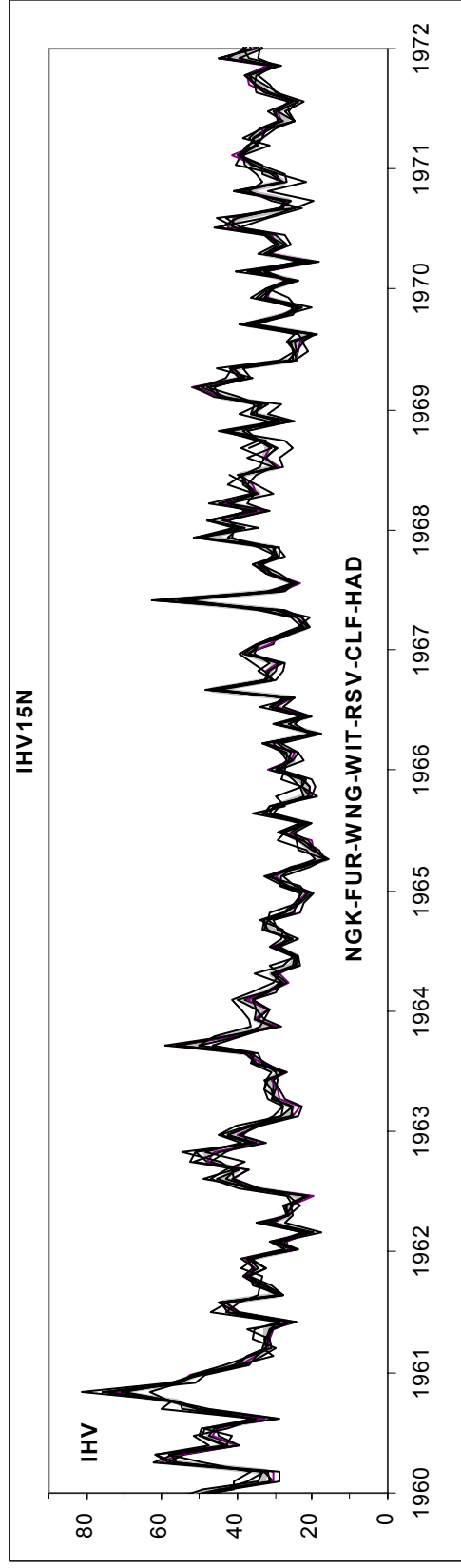


Figure 8

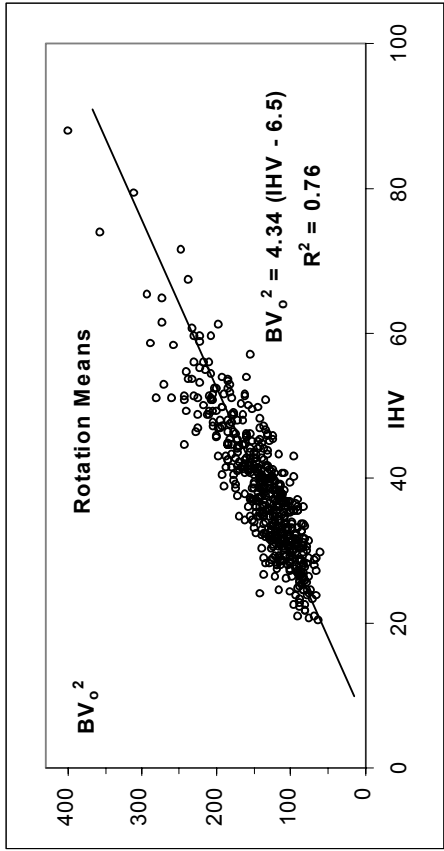


Figure 9a

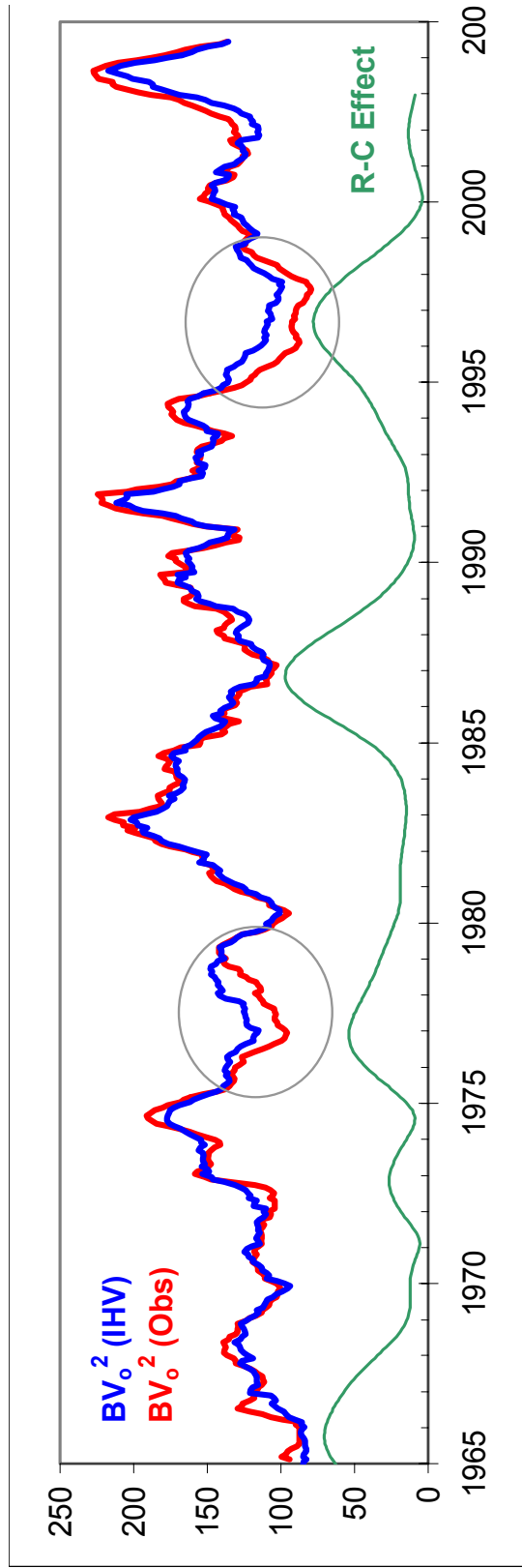


Figure 9b

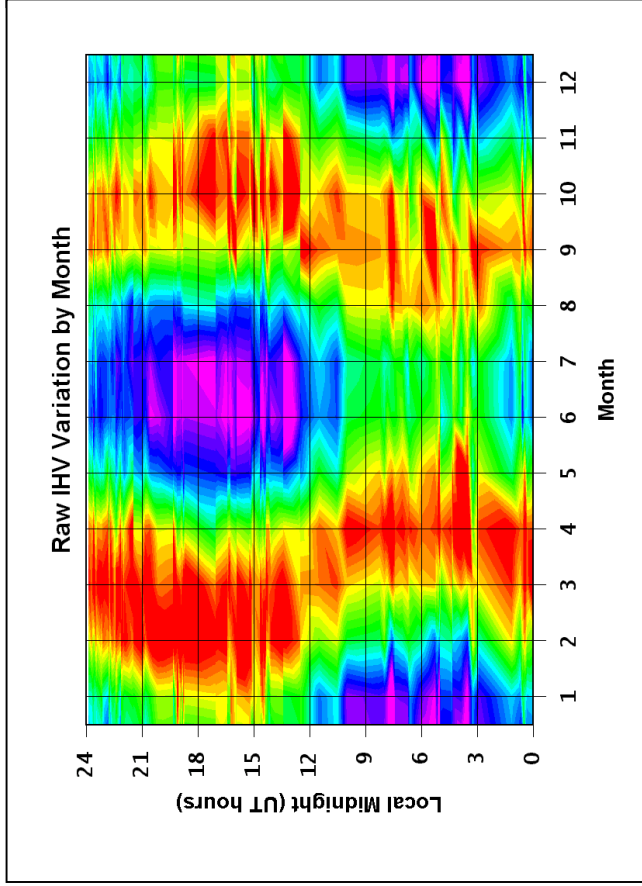


Figure 10a

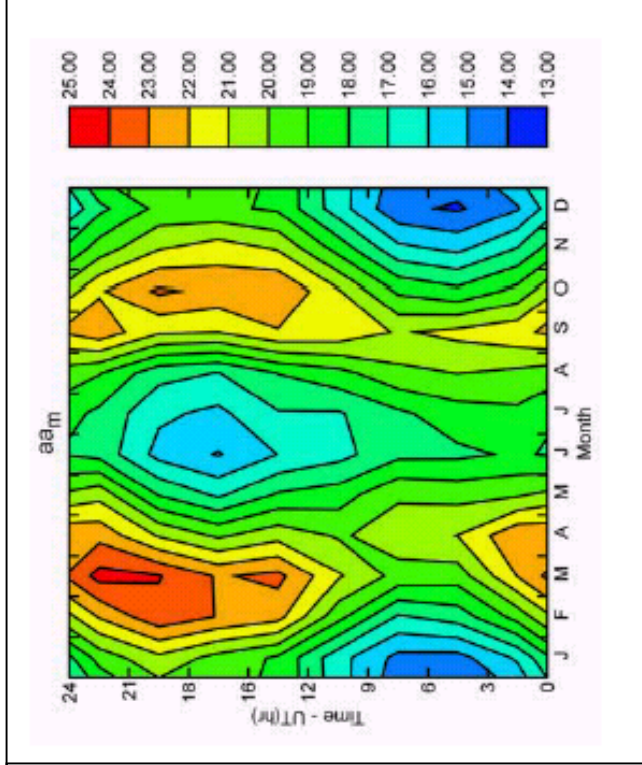


Figure 10b

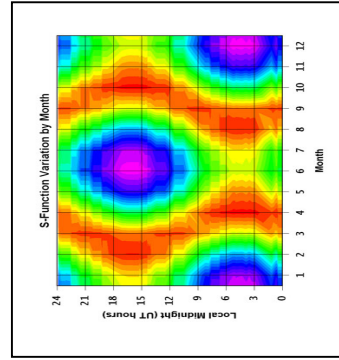


Figure 10c

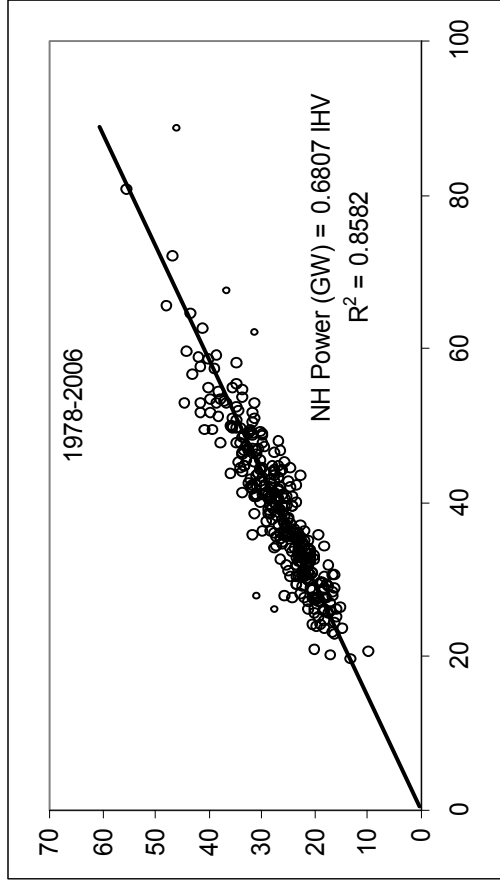
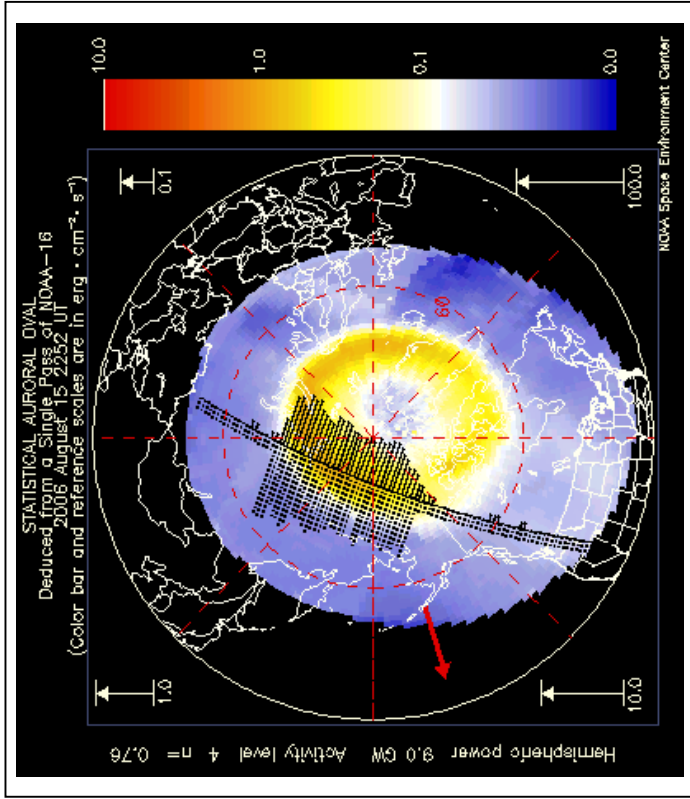
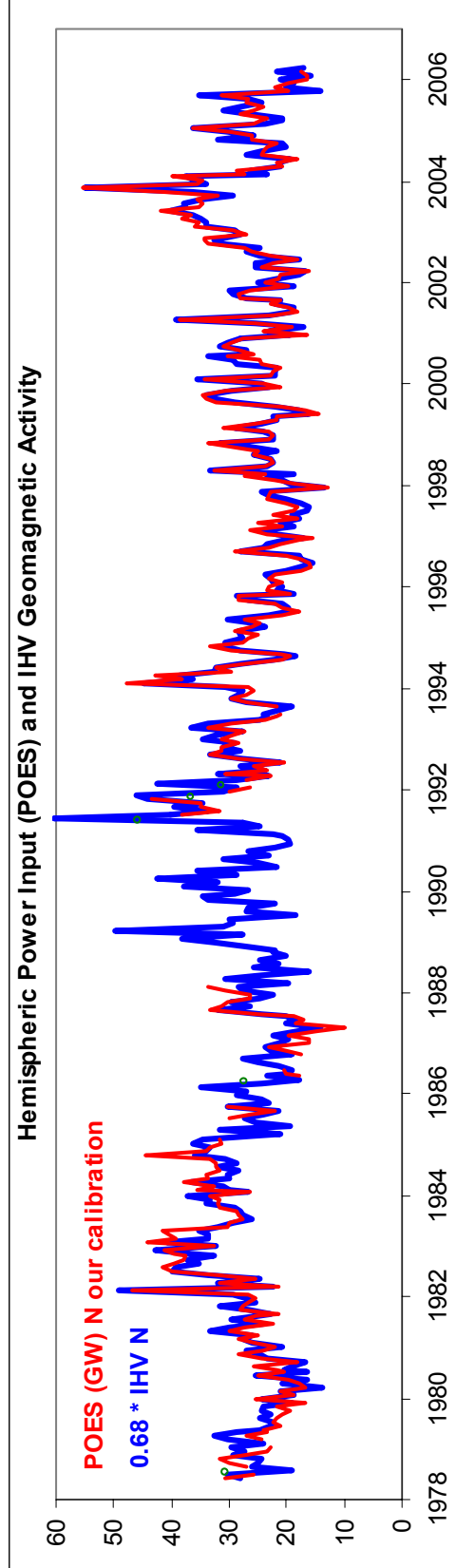


Figure 11a (left)
 Figure 11b (above)
 Figure 11c (below)



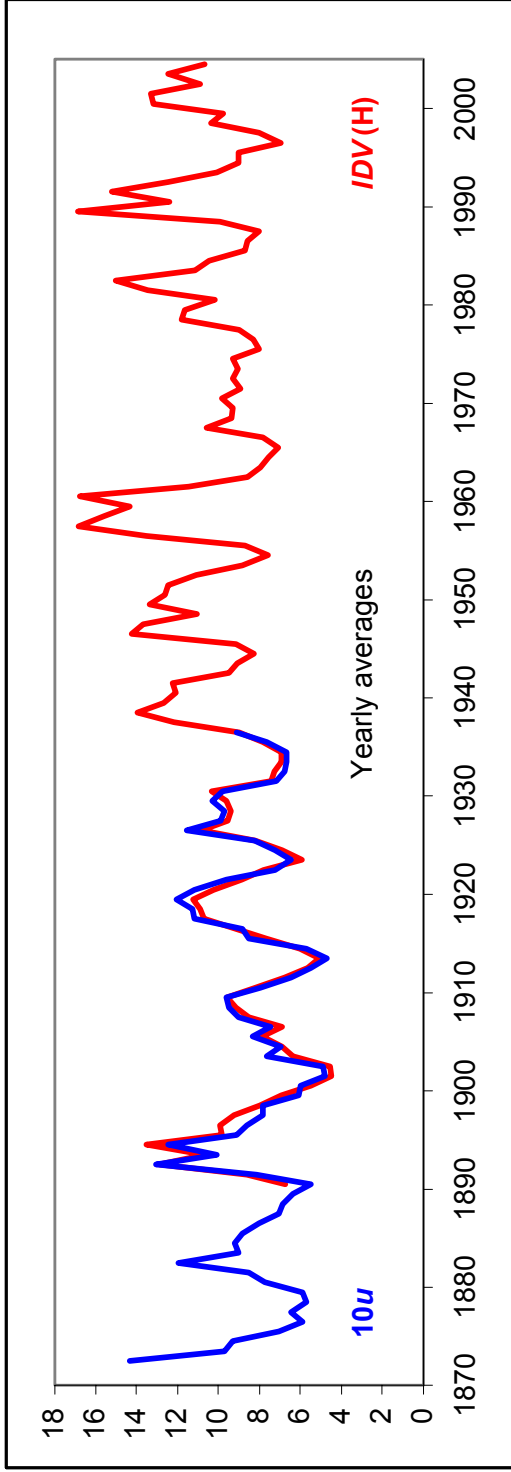


Figure 12

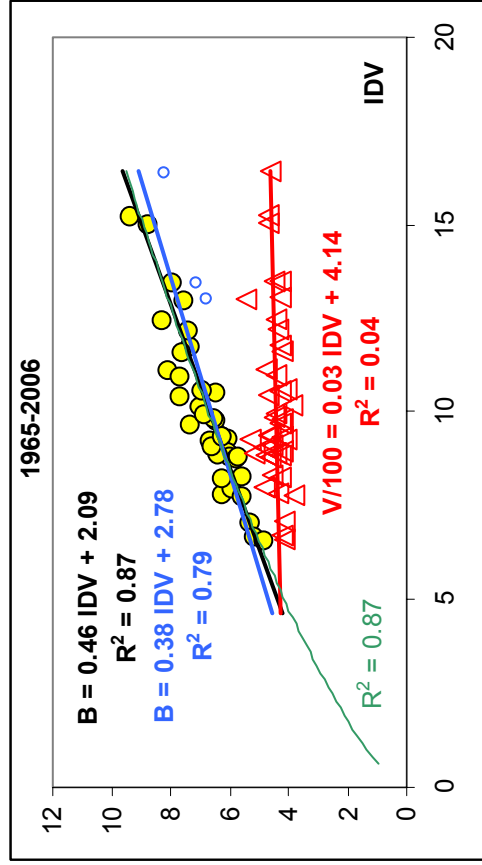


Figure 13

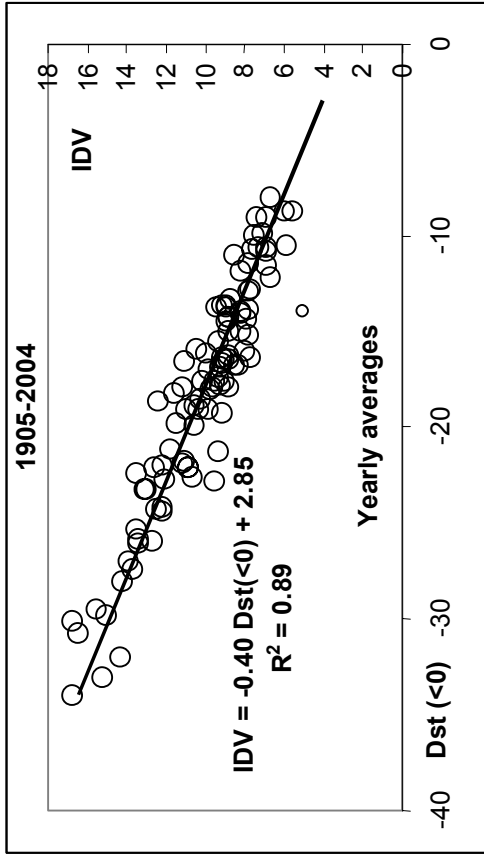


Figure 14a

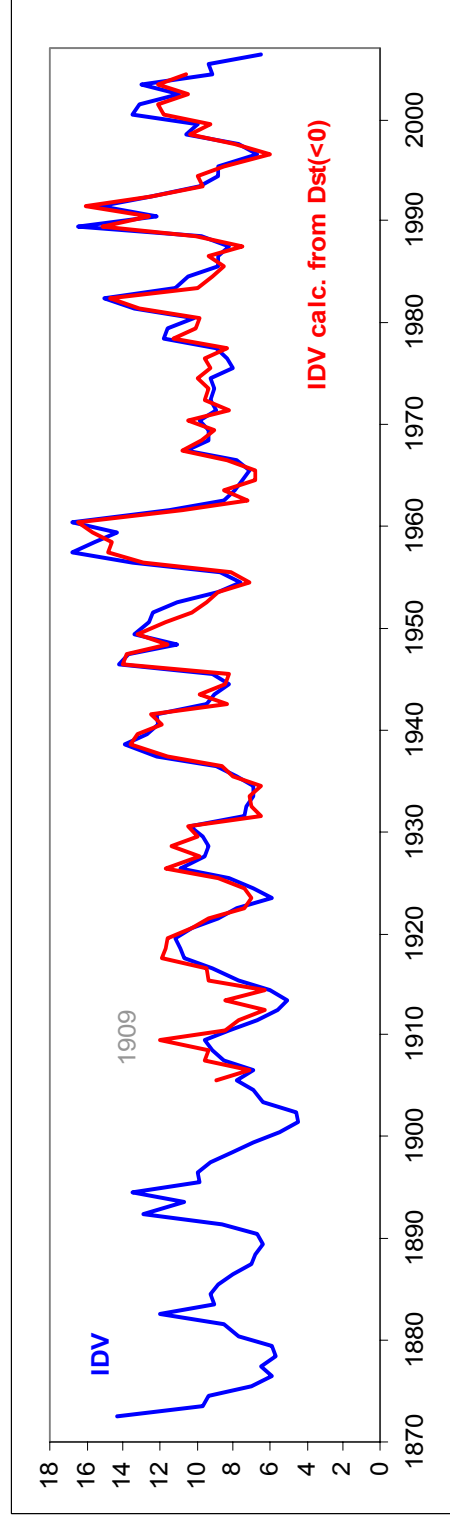


Figure 14b

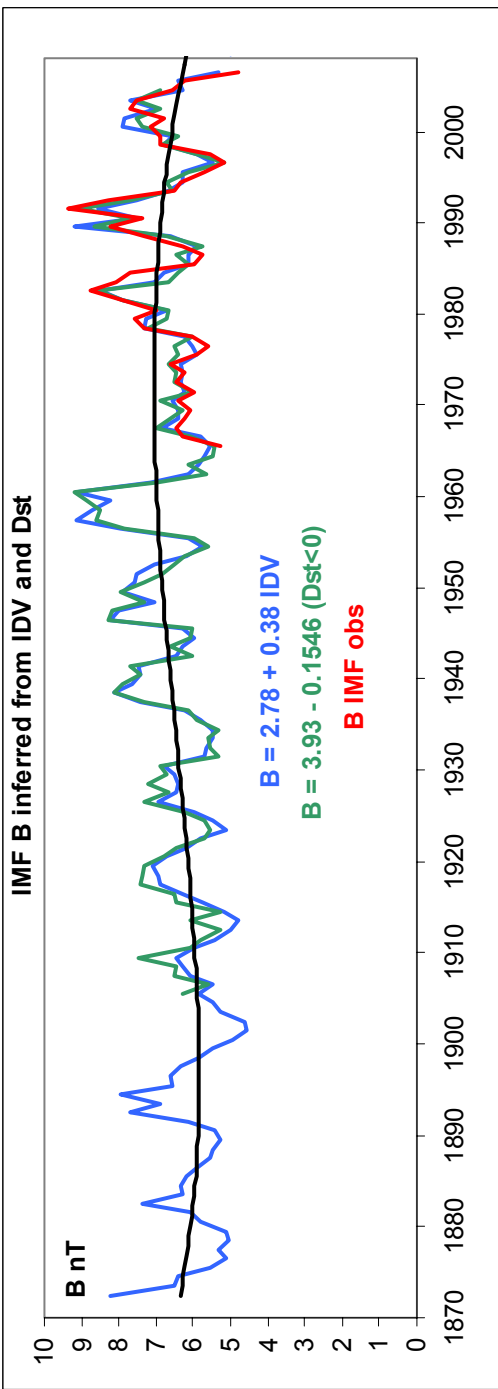


Figure 15

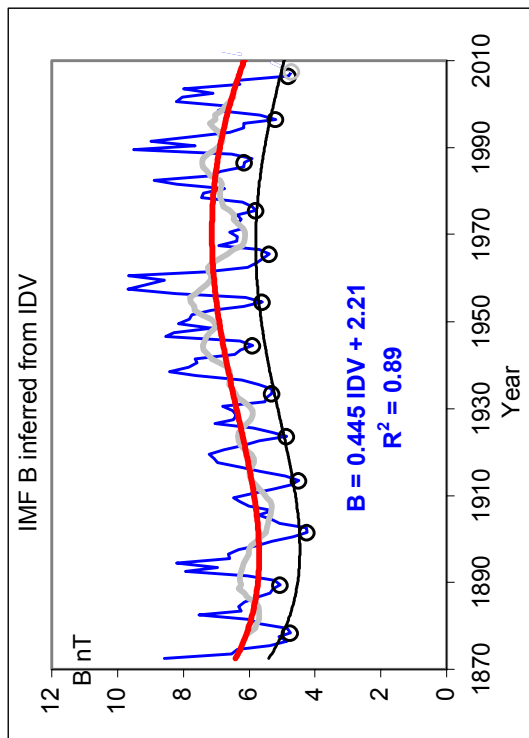


Figure 16

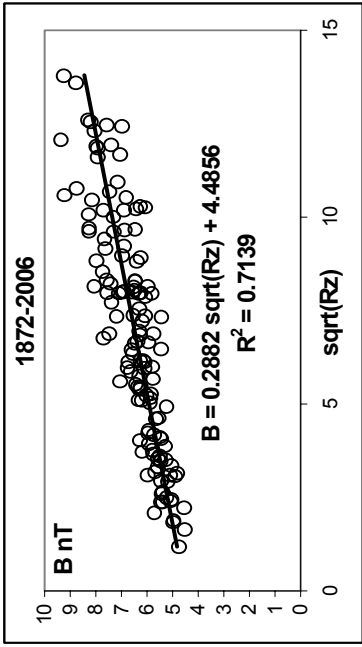


Figure 17a

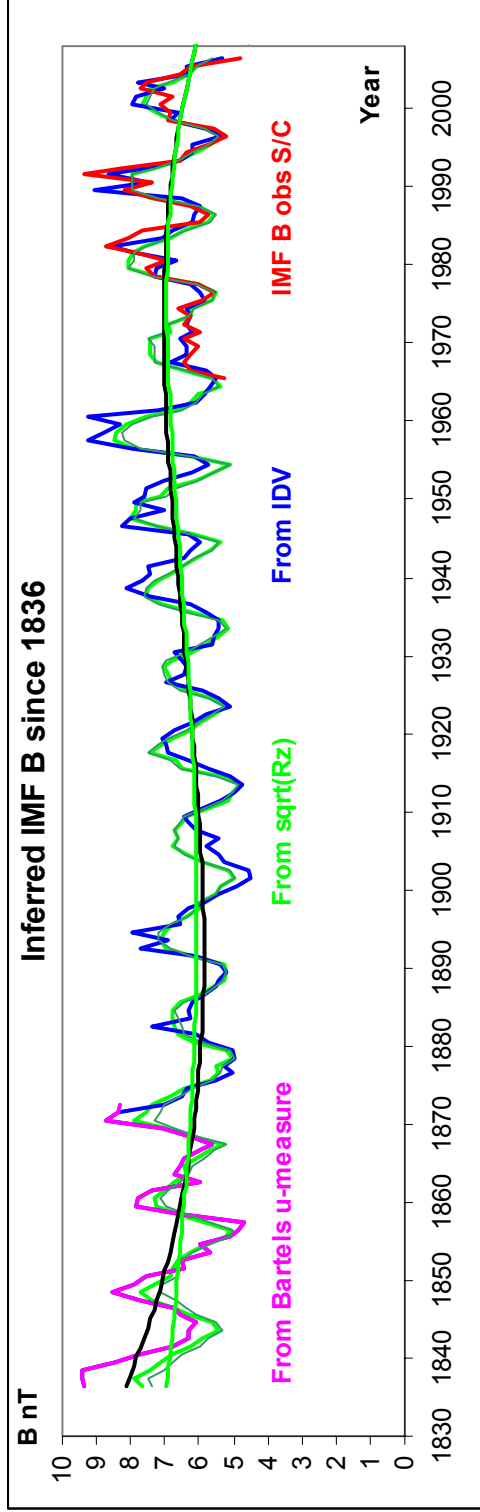


Figure 17b

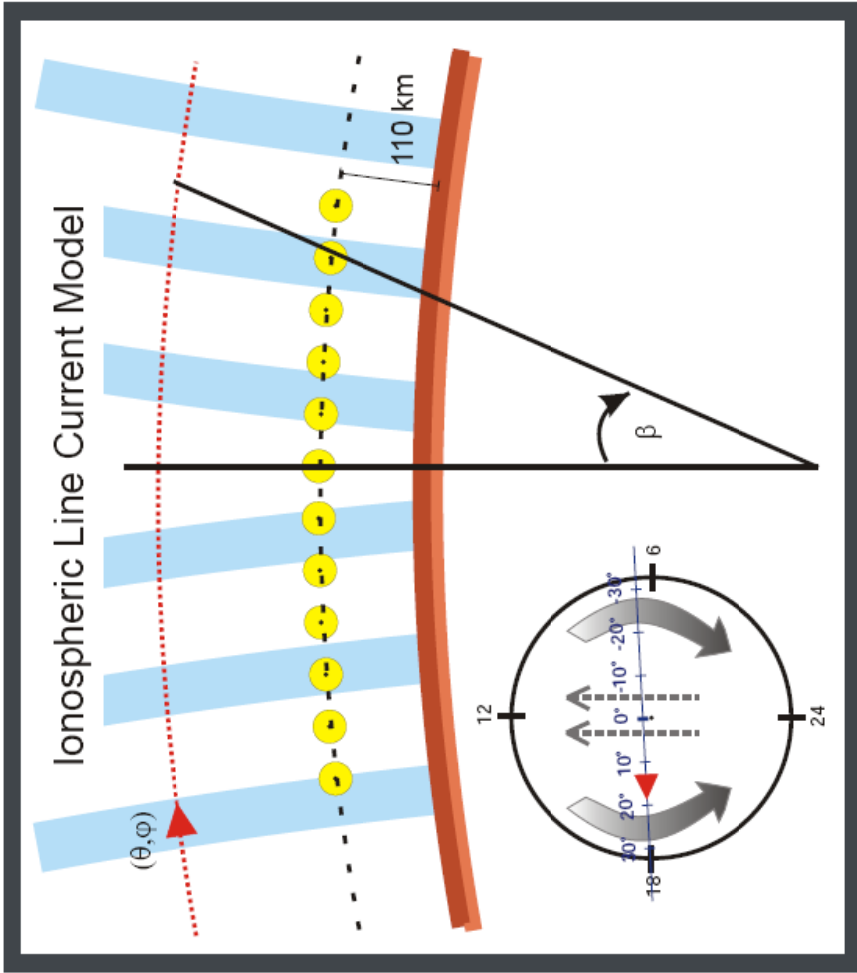
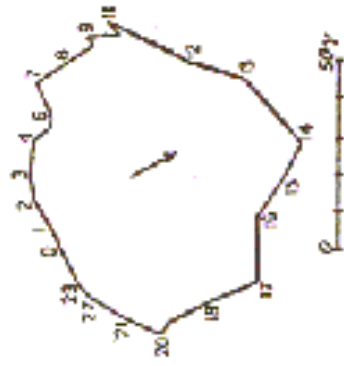


Figure 18



Kingua Fjord 1882-1883

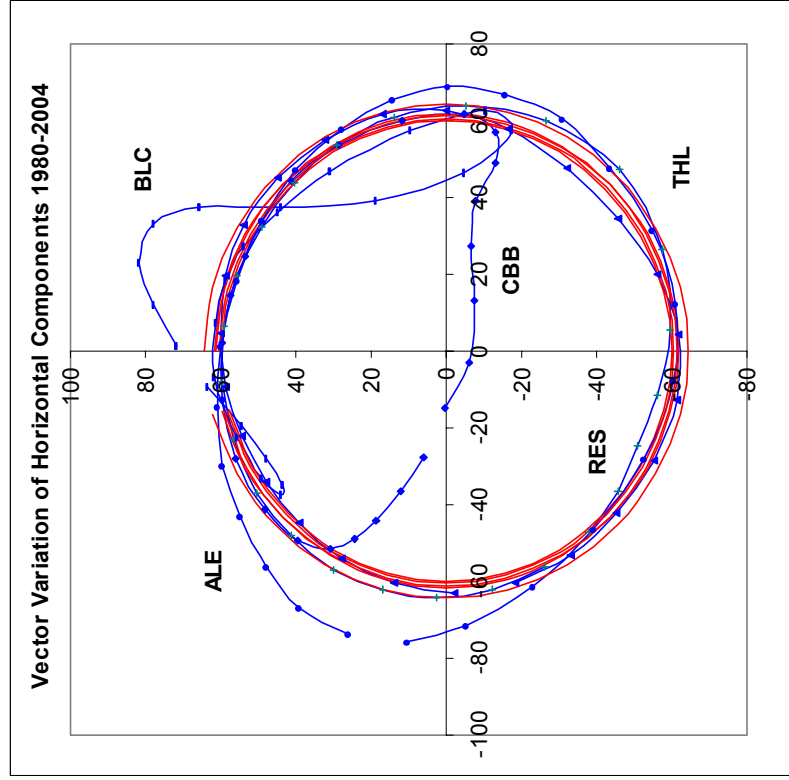


Figure 19a (top)

Figure 19b (bottom)

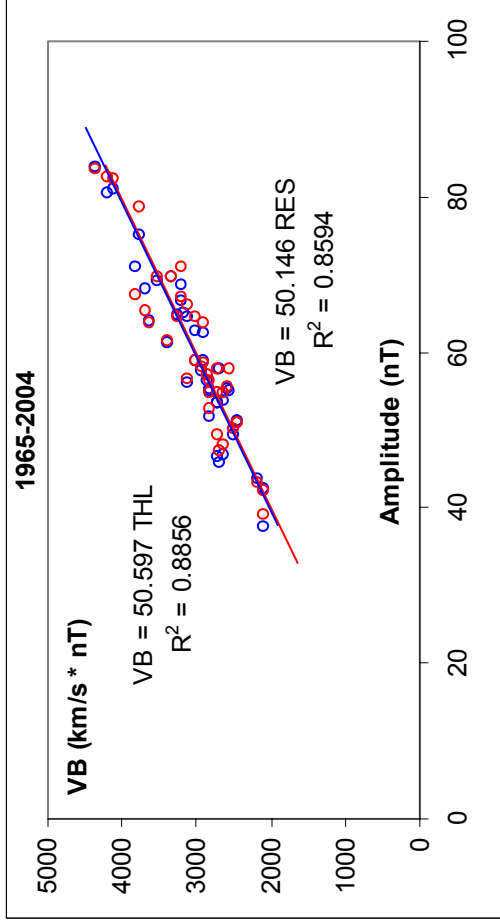


Figure 20a

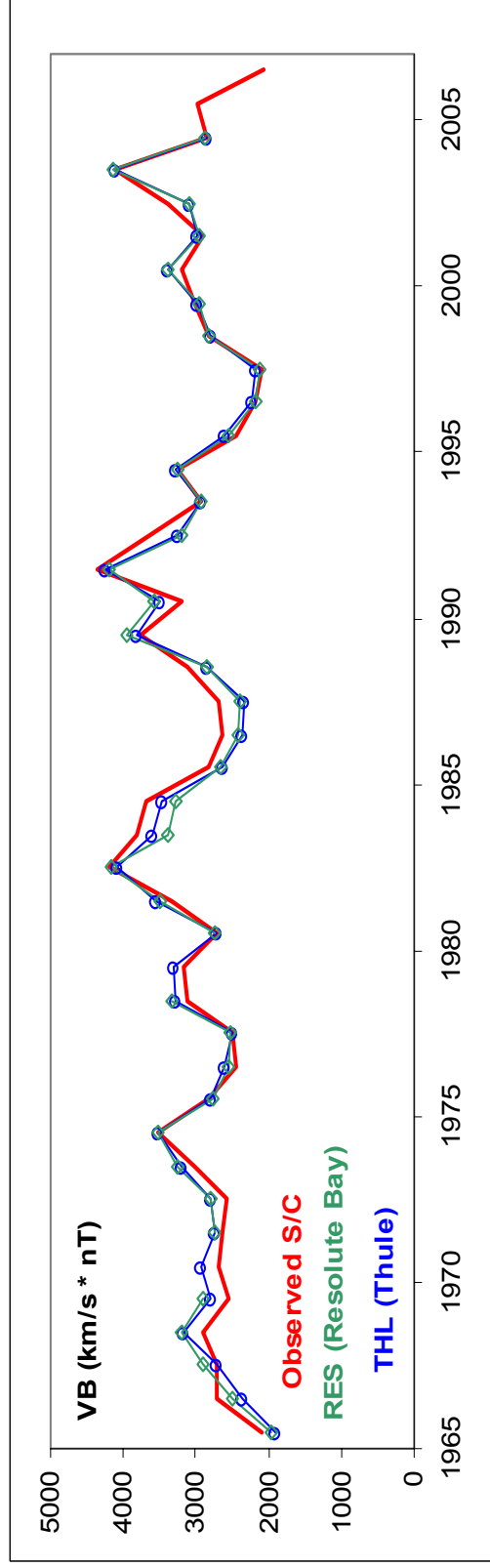


Figure 20b

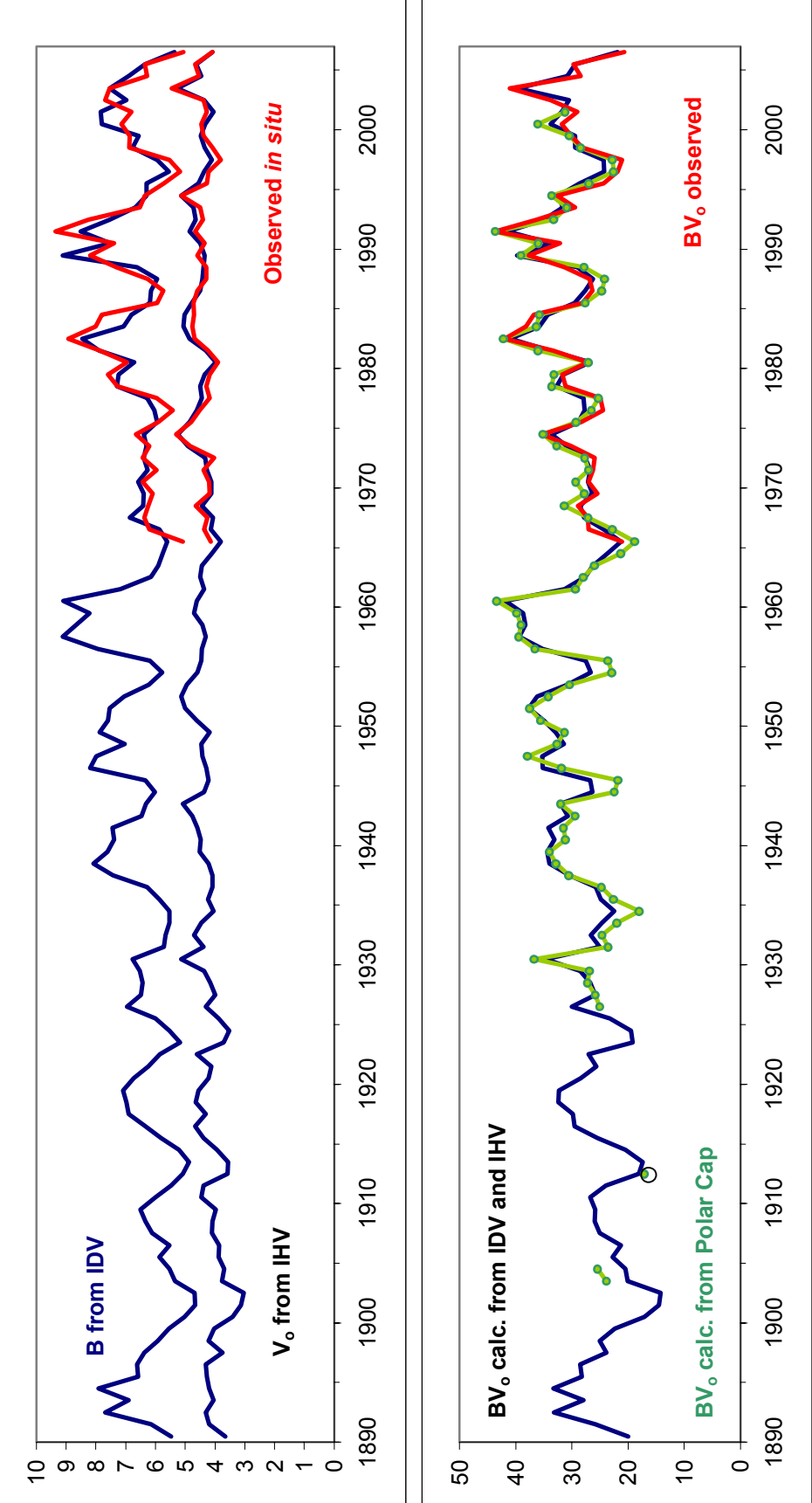


Figure 21

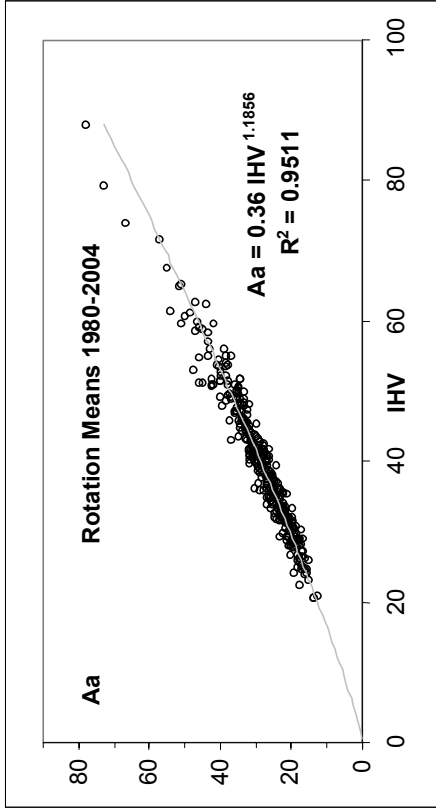


Figure 22

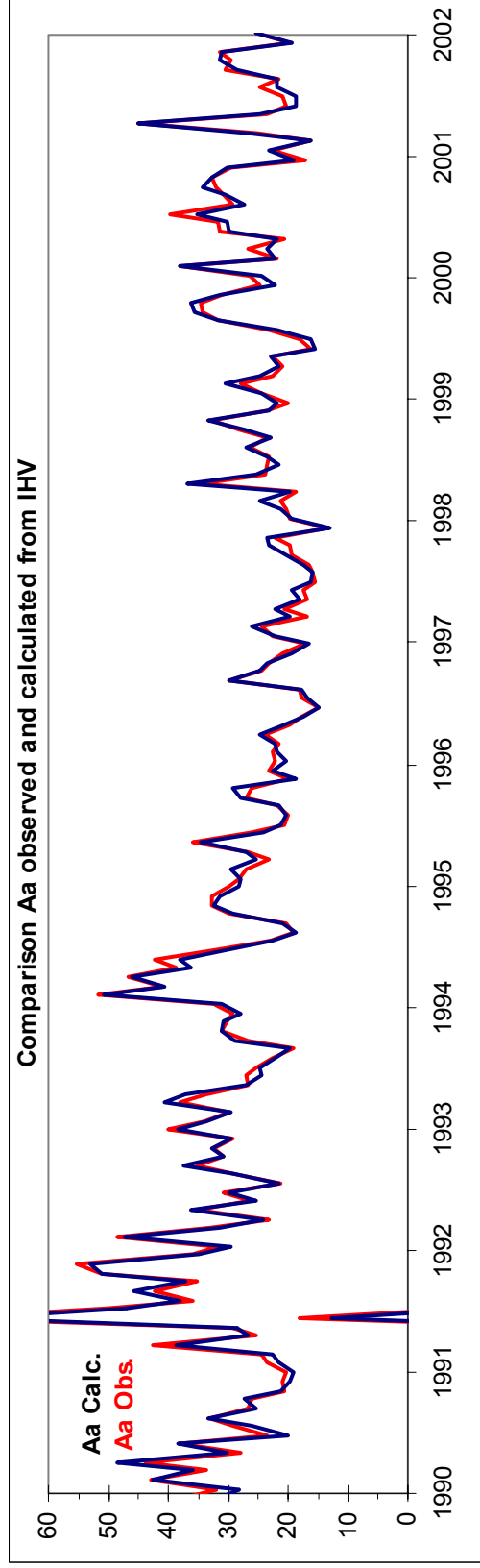


Figure 23

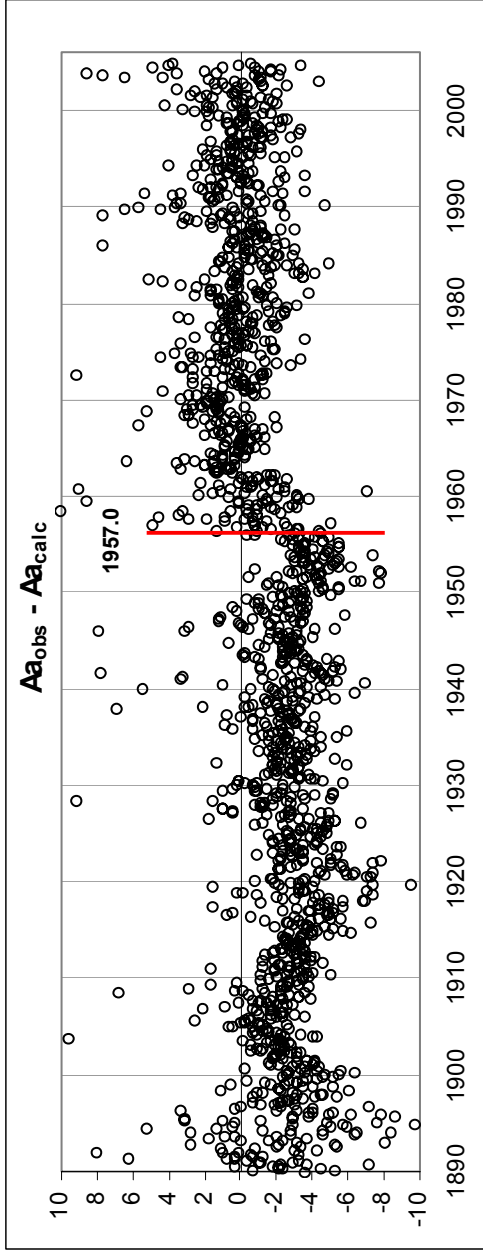


Figure 24

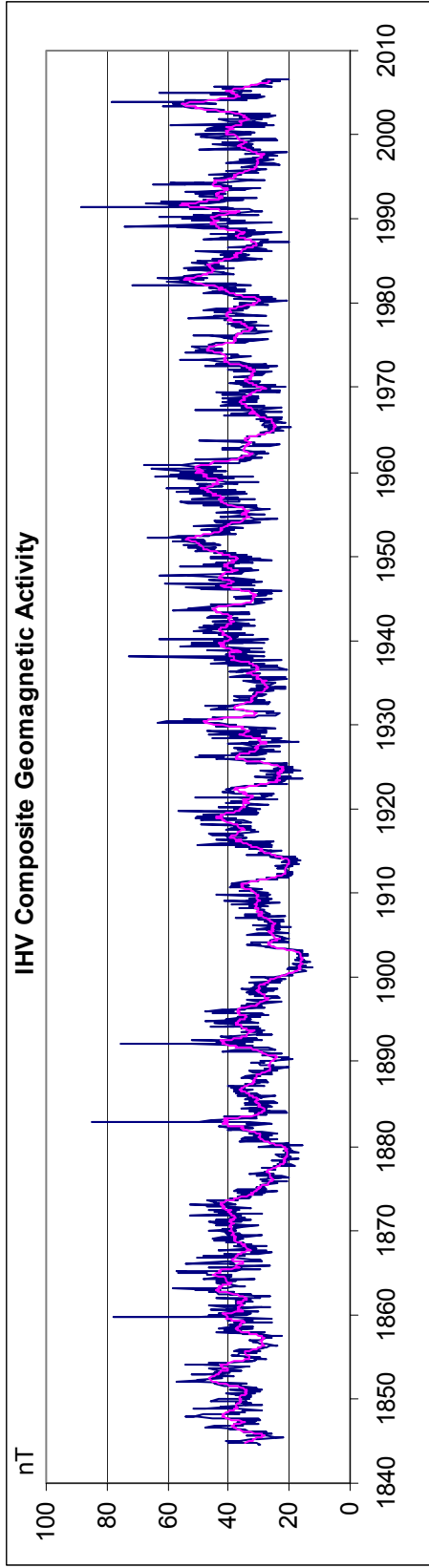


Figure 25

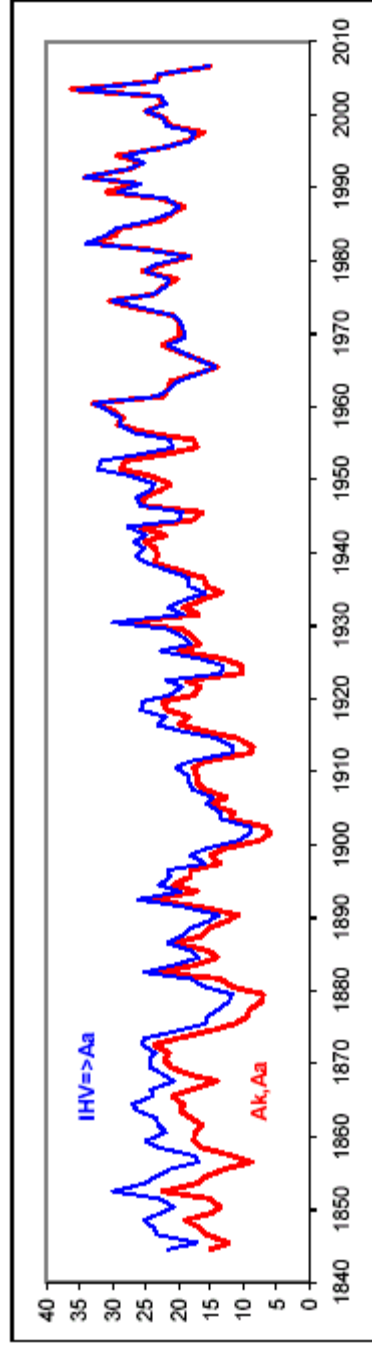


Figure 26